

# A Deep Learning Architecture for Passive Microwave Precipitation Retrievals using CloudSat and GPM Data

Reyhaneh Rahimi<sup>a</sup>, Sajad Vahedizade<sup>a</sup>, Ardeshir Ebtehaj<sup>a,\*</sup>

<sup>a</sup>*Saint Anthony Falls Laboratory and Department of Civil Environmental and Geo- Engineering, University of Minnesota, Minneapolis, MN, 55455 USA.*

---

## Abstract

This paper presents an algorithm that relies on a series of dense and deep neural networks for passive microwave retrieval of precipitation. The neural networks learn from coincidences of brightness temperatures from the Global Precipitation Measurement (GPM) Microwave Imager (GMI) with the active precipitating retrievals from the Dual-frequency Precipitation Radar (DPR) onboard GPM as well as those from the *CloudSat* Profiling Radar (CPR). The algorithm first detects the precipitation occurrence and phase and then estimates its rate, while conditioning the results to some key ancillary information including parameters related to cloud microphysical properties. The results indicate that we can reconstruct the DPR rainfall and CPR snowfall with the detection probability of more than 0.95 while the probability of false alarm remains below 0.08 and 0.03, respectively. Conditioned to the occurrence of precipitation, the unbiased root mean squared error in estimation of rainfall (snowfall) rate using DPR (CPR) data is less than 0.8 (0.1) mm hr<sup>-1</sup> over oceans and land. Beyond methodological developments, comparing the results with ERA5 reanalysis and official GPM products demonstrates that the uncertainty in global satellite snowfall retrievals continues to be large while there is a good agreement among rainfall products. Moreover, the results indicate that CPR active snowfall data can improve passive microwave estimates of global snowfall while the current CPR rainfall retrievals should only be used for detection and not estimation of rates.

*Keywords:* Remote Sensing, Precipitation, Passive Microwave, Global Precipitation Measurement (GPM), CloudSat, Deep Learning

---

\*Corresponding Author

*Email address:* [ebtehaj@umn.edu](mailto:ebtehaj@umn.edu) (Ardeshir Ebtehaj )

---

## 1. Introduction

Precipitation processes play a vital role in space-time dynamics of global water and energy cycle (Kidd and Huffman, 2011; Levizzani and Cattani, 2019). Spatiotemporal variability of precipitation and its phase change affect availability of water resources to ecosystem and society – impacting decision making across a wide range of socioeconomic sectors, especially under a changing climate (Tamang et al., 2020; Qin, 2021). Ground-based rain gauges and precipitation radars are not available over oceans and hardly provide a global picture of overland variability of precipitation. These networks are sparse, especially over remote areas with complex terrains, and their measurements are subject to a large-degree of uncertainty due to variety of reasons such as wind-induced under-catch losses of rain gauges (Fuchs et al., 2001; Duchon and Biddle, 2010) or topographic blockage of ground-based radars. Remote sensing from space has promised to cope with these shortcomings and provide a quasi-global picture of precipitation variability (Rasmussen et al., 2012; Guilloteau et al., 2021); however, there are still technical and knowledge gaps that need to be addressed – especially with respect to monitoring of global snowfall.

Observations provided by passive and active sensors onboard the satellites have been instrumental for almost four decades to expand our understanding of the role of precipitation and its variability in the global hydrologic cycle (Olson et al., 1996; Kummerow et al., 1998; Grecu and Olson, 2006; Sorooshian et al., 2011; Kirschbaum et al., 2017; Skofronick-Jackson et al., 2017). The passive microwave (PMW) brightness temperatures (TB) with wavelengths ranging from 10 to 200 GHz are sensitive to the columnar integrated precipitable water content (Petty, 1994; Skofronick-Jackson et al., 2004; Kummerow et al., 2001). Over radiometrically cold oceans, the observed TBs increase in response to raindrop emission at frequencies below the 60 GHz oxygen absorption line. Consequently, low-frequency channels  $\leq 37$  GHz have been widely used for detection of rainfall over oceans (Bauer et al., 2001; Kummerow et al., 2001; Petty, 2013b; Ebtehaj et al., 2015a). Over higher frequencies, where wavelengths approach to the size of the ice particles, the observed TBs decrease as the upwelling surface emission is scattered by the atmospheric constituents – especially ice particles. Therefore, frequencies above 80 GHz have been employed to detect ice clouds

and snowfall (Bennartz and Petty, 2001; Bennartz and Bauer, 2003; Petty and Huang, 2010; Skofronick-Jackson and Johnson, 2011).

A more direct measurement of precipitation microphysics can be obtained from active precipitation radars, which rely upon measurements of the backscattered power of the transmitted electromagnetic waves due to volume scattering of hydrometeors (Iguchi et al., 2012; Toyoshima et al., 2015; Grecu et al., 2016; Heymsfield et al., 2018). Among existing satellites, the Global Precipitation Measurement (GPM, (Hou et al., 2014)) core satellite launched in 2014 as well as the CloudSat satellite (2006-present, (Stephens et al., 2002)) have provided frequent passive and active observations of near-global precipitation.

The GPM core satellite carries a microwave imager (GMI, 10–187 GHz) and a Ku-Ka (13–35 GHz) band Dual-Frequency Precipitation Radar (DPR) (Skofronick-Jackson et al., 2017) with a coverage of 65° S-N. The GMI scans an outer swath width of 931 km with a mean footprint resolution ranging from 25 km at 10.65 GHz to 6 km at 183.3±7 GHz channels (Draper et al., 2015). The effective field of view of the radiometer varies from 19.4×32.1 km to 3.8×5.8 km (along-scan×cross-scan) at 10.65 GHz and 183.31±7 GHz, respectively. The DPR provides temporally less frequent reflectivity values with an approximate footprint of 5 km resolution over a swath width of 245 km at both Ka and Ku bands.

On the other hand, the W-band (94 GHz) Cloud Profiling Radar (CPR, 2006-present) onboard the CloudSat (Stephens et al., 2002; L’Ecuyer and Jiang, 2010) enables probing the cloud and light precipitation profiles with reflectivity values as low as -30 dBZ (Liu, 2008) with an effective vertical resolution of 240 m over a 1.8×1.4 km (along-track×cross-track) spatial resolution within 82° S-N. Therefore, despite extremely low temporal resolution of CPR, it can be considered as one of the most accurate spaceborne instruments for sensing light precipitation events (Behrangi et al., 2016; Kulie and Milani, 2018; Bennartz et al., 2019).

Coincident observations of both active radars and passive microwave radiometers have been used to develop PMW precipitation retrieval algorithms (Kummerow et al., 1996; Skofronick-Jackson et al., 2003; Grecu et al., 2004; Kummerow et al., 2011; Ebtehaj et al., 2015c; Turk et al., 2018; Munchak et al., 2020). Coincidences of GMI and DPR have been commonly used in the context of Bayesian inference models for PWM precipitation retrievals (Kummerow et al.,

2001; Petty, 2013a; Kummerow et al., 2015; Grecu et al., 2016; Ebtehaj and Kummerow, 2017a). The Bayesian algorithms often match the observed TBs with an *a priori* database that links a statistically representative number of TBs to their radar precipitation profiles. This matching enables to decide about the occurrence and phase of precipitation in a probabilistic sense. However, recent research suggested that DPR is not sufficiently sensitive in capturing backscattering signatures of light and shallow precipitations as it can only record those events with reflectivity above 12-18 dBZ (Liu, 2008; Hamada and Takayabu, 2016), which roughly correspond to precipitation rate of 0.2-0.5 mm hr<sup>-1</sup> (Skofronick-Jackson et al., 2013; You et al., 2017; Casella et al., 2017).

The W-band CPR can properly capture cloud ice particles, droplets, and snowflakes with reflectively values greater than -30 dBZ. Recently, a body of research has been devoted to developing precipitation and snowfall retrieval algorithms through exploiting GMI and CPR coincidences (Rysman et al., 2018, 2019; Vahedizade et al., 2021; Turk et al., 2021). However, it is important to highlight that as precipitation intensity increases, the CPR reflectivity tends to saturate near 20 dBZ as the size of the hydrometeors becomes significantly larger than the wavelength at W-band (Matrosov and Battaglia, 2009). This saturation often increases the uncertainty of the retrievals as the rain rate becomes higher than 10 mm hr<sup>-1</sup> (L'Ecuyer and Stephens, 2002; Tang et al., 2017).

In parallel to the Bayesian retrieval algorithms, artificial neural networks (ANN) have been deployed for PMW precipitation retrievals largely from infrared satellite observations (Sorooshian et al., 2000; Hong et al., 2004; Tapiador et al., 2004), and to a lesser extent, from microwave bands (Liou et al., 1999; Aires et al., 2001; Sanò et al., 2016, 2018). These ANNs are learning architectures that propagate the input data across a sequence of weighted averaging followed by non-linear operations in a series of layers. To properly adjust the network weights based on the training dataset, a learning algorithm computes gradient vectors that sequentially capture the steepest descent direction towards a (local) minimum of a properly designed cost function. Predictive capabilities of classic ANNs were limited due to two main reasons. First, those networks could not be scaled up to solve large-scale problems due to their fully connected architecture. Second, classic optimization algorithms could not update the network weights for high-dimensional data and where the number of layers and

computational nodes could be staggeringly large (Glorot and Bengio, 2010).

In the last decade, there have been significant advances in learning paradigms including stochastic (Bottou, 1991) and batch gradient (Dekel et al., 2012) approaches that efficiently approximate the gradient vector and reduce its dependence on the size of the network and the initial weights. Modern non-degenerative activation functions such as the rectified linear units (ReLU) (Nair and Hinton, 2010) were introduced to avoid vanishing gradient problem and to promote sparsity in the weights. Moreover, to overcome over-fitting, new effective and computationally amenable regularization methods, such the Dropout technique (Srivastava et al., 2014), were proposed. These advances, as well as high-capacity graphical processing units (GPU) have made it possible to increase the number of hidden layers significantly – coining the term “deep learning” – and expand the predictive accuracy of the neural network beyond what was possible in shallow ANNs. Different deep neural networks (DNN) have been developed in recent years (LeCun et al., 2015; Wang and Raj, 2017; Goodfellow et al., 2017), solving numerous problems in signal and image processing such as object detection (Deng et al., 2018; Zhao et al., 2019), image classification (Li et al., 2018, 2019), and speech recognition (Deng et al., 2013; Nassif et al., 2019)) with an unprecedented accuracy.

Recently, there has been a renewed interest to advance PMW retrievals of precipitation and other atmospheric constituents through DNN models. In one of the early attempts (Pfreundschuh et al., 2018), a Quantile Regression Neural Networks (QRNN) was developed to estimate cloud physical properties using observations by the Moderate Resolution Imaging Spectroradiometer (MODIS, (Platnick et al., 2003)). In (Tang et al., 2018), a shallow multilayer perceptron (MLP) network with two hidden layers was proposed that used re-analysis data as well as coincidences of GMI TBs with both DPR and CPR retrievals of precipitation to obtain passive estimates of high latitude rain and snow. The proposed architecture used the tangent sigmoid as an activation function and the Levenberg–Marquardt algorithm (Moré, 1978) to update the network weights. A deep MLP network was employed in (Chen et al., 2020) to retrieve the rainfall information using both infrared and PMW data and its performance was validated over the Dallas–Fort Worth metropolplex, Texas, United States. More recently, to extract spatial features of precipitation, a U-Net convolutional

neural network was developed (Gorooh et al., 2022) – allowing high resolution retrievals through ingesting data from infrared and PMW satellites over different land-cover types.

Building upon previous research, this paper aims to answer the following key questions: Can DNN architectures lead to PMW retrievals with an accuracy beyond the existing Bayesian algorithms that rely on  $k$ -nearest matching (Ebtehaj et al., 2015a; Takbiri et al., 2019; Vahedizade et al., 2021)? How can physically relevant variables such as cloud water content be incorporated in the retrievals and what would be their effects on the uncertainties? Where and to what extent can CPR data lead to improved retrieval of precipitation at different phases beyond those learned from DPR data? Can deep neural networks disentangle the precipitation and snow-cover microwave signatures without any given information about the presence of snow on the surface?

To answer the above questions, the paper has the following contributions. (i) This study uses a pixel-level dense DNN architecture based on two databases of coincidences of GMI–DPR as well as GMI–CPR. (ii) The proposed architecture has sequential detection and estimation modules to first identify the precipitation occurrence and its phase (i.e., rain vs snow) and then estimate its rate. (iii) Physical variables including clouds liquid and ice water path, total precipitable water, 2-m air temperature, and convective potential energy (CAPE) are used along with the TB values for detection of precipitation and its phase through a multinomial classification scheme. (iv) The power of the DNN and  $k$ -nearest neighbor matching is combined to promote localization in estimation of precipitation rate. (v) The DNNs employ ReLU activation functions (Nair and Hinton, 2010), batch normalization (Ioffe and Szegedy, 2015), Dropout regularization (Srivastava et al., 2014), and the Root Mean Squared Propagation (RMSProp) (Hinton et al., 2012) algorithm to update the network weights using mean squares (absolute) error loss functions for retrieval of rainfall (snowfall).

The paper is organized as follows. Section 2 describes the data including the GPM and CloudSat products as well as the ERA5 reanalysis data from the European Centre for Medium-Range Weather Forecasts (ECMWF) (Hersbach et al., 2018). Section 3 explains the methodology. The results, findings, and discussions are presented in Section 4. In this section, retrievals and the performance of the proposed DNN are presented and compared

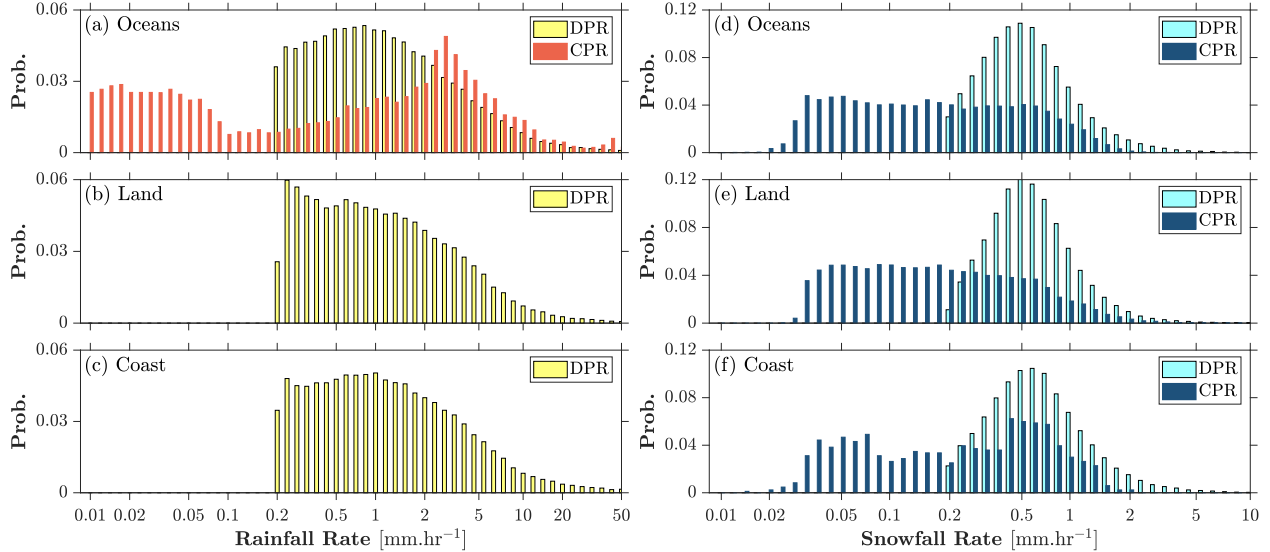


**Fig. 1.** Probability histograms of the GPM DPR and *CloudSat* CPR precipitation over three different surface types defined in the GPROF Algorithm Theoretical Basis Document (ATBD, (Kummerow, 2016)).

with a Bayesian approach (Ebtehaj et al., 2015a) for training based on both DPR and CPR data. Section 5 provides a summary, concluding remarks, and points out to future research directions.

## 2. Data

In this study, we use near-coincident observations of GMI and CPR from March 2014 to August 2016 (Turk et al., 2021), coincidences of GMI and DPR data in 2015, as well as the ERA5 reanalysis data from the European Centre for Medium-Range Weather Forecasts (ECMWF, Hersbach et al., 2018). Note that the samples size of CPR coincidences is much smaller than the DPR and thus we need more years to collect adequate CPR data for robust training of the algorithm. The Multi-Radar/Multi-Sensor System (MRMS) radar precipitation (Kirstetter et al., 2012; Zhang et al., 2016) as well as precipitation products from the Goddard Profiling Algorithm (Kummerow et al., 2015, V07) are used for cross comparison and retrieval assessment.

The GMI-CPR coincidences rely on the level-II CloudSat products (R05) including the 2C-PRECIP-COLUMN (Haynes et al., 2009) and the 2C-SNOW-PROFILE (Wood et al., 2013, 2014) that respectively contain near-surface rain and snowfall rates. To avoid ground-

clutter contamination over complex elevated terrains, the near-surface snowfall rate is reported at 3rd (5th) radar bin above the oceans (land) at 720 m (1200 m) above the surface (Kulie et al., 2010). In these coincidences, rainfall retrievals over land and coastal areas are not available as they were not reported in the original CloudSat products.

The 2A-DPR product (Iguchi et al., 2018), retrieved from Ku-band reflectivity, includes the near-surface precipitation phase and its intensity. Furthermore, ancillary information of 2-m air temperature, cloud liquid and ice water paths, and convective available potential energy (CAPE) are added to all coincidences using the ERA5 reanalysis products (Hersbach et al., 2018) – available at spatial resolution of 31 km. It should be noted that the DPR algorithm uses precipitation phase at the lowest radar range gate uncontaminated by surface clutter, which may be 0.5–2.0 km above the surface (even over oceans). The profile of phase (ice, melting, or liquid) is determined via a bright band detection algorithm using the temperature profile provided by ancillary data Japan Meteorological Agency’s Global Analysis (GANAL, Yamaguchi and Komori, 2009). Therefore, phase changes between the actual surface and DPR “near surface” are definitely possible (Skofronick-Jackson et al., 2019). Throughout, the GMI–DPR and GMI–CPR databases are divided based on different surface types including ocean, land, and coastal zones using the information provided by the Goddard Profiling Algorithm (GPROF, Kummerow, 2016).

In summary, the *a priori* database contains  $40\text{E}+6$  ( $5.5\text{E}+6$ ) number of GMI-DPR (GMI-CPR) coincidences over oceans. The number of coincidences are  $6.5\text{E}+6$  ( $2\text{E}+6$ ) over land and  $2\text{E}+6$  ( $6\text{E}+5$ ) over coastal zones. These databases will be used to train, validate, and test the proposed retrieval algorithm. The GMI observations are from the calibrated TBs (1C.GPM.GMI, V05) (Berg, 2016). The coincidences with DPR are reported at 5 km spacing where both S1 (10–89 GHz) and S2 (166–183 GHz) GMI channels have overlapping observations.

Probability histograms of the collected CPR and DPR precipitation data at two different precipitation phases are shown over the three surface types in Fig. 1. The CPR rainfall data over ocean represent a bimodal distribution. The dominant mode of the distribution is around  $3 \text{ mm hr}^{-1}$ , which is  $\sim 2 \text{ mm hr}^{-1}$  greater than the mode of the DPR data. The distribution of CPR snowfall is much wider than DPR and has a significantly smaller mean

values  $\sim 0.2 \text{ mm hr}^{-1}$  across all surface types than the DPR counterpart with a mean around  $0.5 \text{ mm hr}^{-1}$ .

### 3. Methodology

Focusing on the PMW precipitation retrievals, we briefly review the basics of the classic Bayesian retrieval algorithms. Then, we elaborate upon the design of the proposed DNN model and its connection with a particular Bayesian model presented in (Ebtehaj et al., 2015a).

#### 3.1. Bayesian Retrieval Algorithms

Atmospheric radiative transfer (RT) models (Liu and Curry, 1993; Evans and Stephens, 1995; Liu and Curry, 1997) require a large number of parameters and input variables of atmospheric column as well as spectral surface emissivity values to simulate the TBs at top of the atmosphere. Inversion of these forward models is often severely ill-posed as precipitation rate becomes non-uniquely related to the observed TBs at a few frequency channels. To cope with this non-uniqueness, a Bayesian class of inversion models has emerged (Kummerow et al., 2001, 2011; Petty and Li, 2013; You et al., 2015; Ebtehaj et al., 2015b, 2016) that learns from an *a priori* database of precipitation profiles and their corresponding simulated/observed TBs.

Conceptually, given a pixel-level vector of TBs, a Bayesian algorithm attempts to isolate a subset of physically similar vectors of TBs in the database and retrieve statistics of their associated precipitation profiles. Physically similar TBs can be isolated by subsetting the database based on the known underlying physical conditions (Kummerow et al., 2015; You et al., 2015), low-dimensional matching of pseudo channels (Petty, 2013a; Turk et al., 2018), and/or through a multi-frequency  $k$ -nearest neighbor ( $k$ NN) matching (Ebtehaj et al., 2015a,c; Takbiri et al., 2019; Guilloteau and Foufoula-Georgiou, 2020; Ebtehaj et al., 2020; Vahedizade et al., 2021). Here we provide a brief description of the  $k$ NN approach that we will combine its localized linear embedding properties with the proposed deep learning architecture.

In particular, let us assume that a collection of  $M$  vectors of TBs, namely  $\mathbf{T}_b \in \mathbb{R}^n$ , at  $n$  frequency channels, and their corresponding precipitation properties  $\mathbf{p} \in \mathbb{R}^3$ , including the near-surface precipitation occurrence, phase, and rate are collected in a database  $\mathcal{B}_\ell = \{(\mathbf{T}_{b_i}, \mathbf{p}_i)\}_{i=1}^M$ , over the  $\ell^{\text{th}}$  surface type that is either ocean, land, or coast. Given an observed pixel-level vector of  $\mathbf{T}_b^{\text{obs}}$  over the surface type  $\ell$ , its  $k$ -nearest neighbors  $k \ll M$  will be identified in  $\mathcal{B}_\ell$  using the Euclidean or the Mahalanobis distance (Ebtehaj et al., 2020).

The isolated subset  $\{\mathbf{T}_{b_i}^{\text{t}}\}_{i=1}^k$  of  $k$ -nearest neighbors and their corresponding precipitation properties  $\{\mathbf{p}_i^{\text{t}}\}_{i=1}^k$  can be used to *detect* the occurrence and phase of precipitation associated with  $\mathbf{T}_b^{\text{obs}}$  through a nested majority vote rule. Specifically, if majority of  $\{\mathbf{p}_i^{\text{t}}\}_{i=1}^k$  are precipitating,  $\mathbf{T}_b^{\text{obs}}$  will be labeled as precipitating. The phase is then decided through a similar majority vote rule among the neighboring precipitating profiles.

Given the precipitation occurrence and phase of  $\mathbf{T}_b^{\text{obs}}$ , the inverse model linearly combines the precipitating neighbors with the same precipitation phase (i.e., snow vs. rain) to *estimate* the near-surface precipitation rate  $\hat{r} = \sum_{i=1}^{k'} \omega_i \times r_i^{\text{t}}$ , where  $r_i^{\text{t}}$  denotes the  $i^{\text{th}}$  neighboring near-surface rate,  $\omega_i$  is a weight, and  $k' \leq k$  is the number of precipitating profiles with the same phase. The weights need to sum to one and can be obtained either through a look-up table (Petty and Li, 2013), an inverse distance weighting interpolation (Kummerow et al., 2001) or a constrained regularized least-squares (Ebtehaj et al., 2015b).

### 3.2. DIEGO: Deep-learning precipitation rETrieval alGORithm

#### 3.2.1. Basics of the Design and Architecture

As briefly explained, a DNN is a universal approximator that establishes a functional relationship between any learnable set of input-output data points (Atkinson and Tatnall, 1997) through interconnected neural nodes in multiple layers as discussed in numerous seminal works (Rosenblatt, 1958; Bishop, 2006; Bengio, 2009; LeCun et al., 2015; Goodfellow et al., 2017). Here we briefly explain this structure tailored to the PMW precipitation retrieval problem for the sake of completeness. Note that we call the used neural networks “deep” not solely because they have 4 to 6 layers and more than 200 neurons. The reason is that we use modern training and regularization techniques that enable to propagate the information content of data into a large number of layers and train the network with an accuracy beyond

traditional methodologies.

Let us assume that a neural network consists of  $l = 1, \dots, L$  layers, including the input and output layers, where  $l - 1$  and  $l^{\text{th}}$  layers indicate two consecutive hidden layers with  $n$  and  $m$  neurons, respectively. Consider that  $\mathbf{a}^{[l-1]} \in \mathbb{R}^m$  is the output of all neurons in layer  $l - 1$ ,  $\mathbf{W}^{[l-1]} \in \mathbb{R}^{n \times m}$  denotes the weights connecting the layer  $l - 1$  to the layer  $l$ , and  $\mathbf{b}^{[l]} \in \mathbb{R}^m$  contains the biases in layer  $l$ . A fully connected architecture uses repeated application of a nonlinear activation function  $\sigma(\mathbf{W}^{[l-1]}\mathbf{a}^{[l-1]} + \mathbf{b}^{[l]}) : \mathbb{R}^m \rightarrow \mathbb{R}^m$  for all neurons over each layer and pass their outputs to all neurons in the next layer.

Let us assume that we have  $M$  input-output training data points  $\{\mathbf{T}_{b_i}^c, \mathbf{t}_i, r_i\}_{i=1}^M$ . Here, each  $\mathbf{T}_{b_i}^c \in \mathbb{R}^{n+n_s}$  denotes a *concatenated* set of inputs that contains TBs at  $n$  frequency channels as well as  $n_s$  physically relevant state variables (e.g., 2-m air temperature);  $\mathbf{t}_i$  are the labels denoting the state of the atmosphere near the surface (i.e., non-precipitating, raining, snowing); and  $r_i$  is the surface precipitation rate. In this context, for example the outputs from the last layer of a DNN with four layers has the following functional form:

$$\mathcal{F}(\mathbf{T}_{b_i}^c) = \sigma(\mathbf{W}^{[4]}\sigma(\mathbf{W}^{[3]}\sigma(\mathbf{W}^{[2]}\mathbf{T}_{b_i}^c + \mathbf{b}^{[2]}) + \mathbf{b}^{[3]}) + \mathbf{b}^{[4]}),$$

where  $\mathcal{F}(\mathbf{T}_{b_i}^c) \in \mathbb{R}^D$ .

Here, we have a sequence of detection and estimation DNNs analogous to the explanations provided for the Bayesian approach. For a detection DNN (d-DNN), the inputs are cloud liquid (LWP) and ice (IWP) water paths, total columnar water vapor mass (WVP), CAPE, and 2-m air temperature. The output layer has three neurons  $D = 3$  to account for the target labels  $\mathbf{t}_i(\mathbf{T}_{b_i}) = (t_i^1, t_i^2, t_i^3)$ , which is a one-hot vector that encodes near surface atmospheric conditions including “no-precipitating”, “snowing”, and “raining”. For example,  $\mathbf{t}(\mathbf{T}_{b_i}) = [1, 0, 0]^T$  denotes a non-precipitating atmosphere near the surface.

For the estimation DNN (e-DNN) the inputs are  $\mathbf{T}_{b_i} \in \mathbb{R}^n$  and surface precipitation rates associated with its  $k$ -nearest neighbors (i.e.,  $k = 20$ ) in the training databases as described in Section 3.2.4. Feeding the DNN with  $k$ -nearest neighbor TBs help to localize its estimation. Clearly, the output layer has only one neuron  $D = 1$  to estimate the near surface precipitation rate. In this case, there are two different networks for estimating near surface rain and snowfall rates to avoid propagating estimation errors due to the use of

different  $Z$ - $R$  and  $Z$ - $S$  relationships for rainfall and snowfall retrievals respectively.

### 3.2.2. Activation and Cost Functions

Clearly, the output of the network  $\mathcal{F}(\mathbf{T}_{b_i}^c)$  should remain in proximity of  $\mathbf{t}(\mathbf{T}_{b_i}^c)$  (detection) or  $r_i$  (estimation), based on a distance metric. To that end, a *loss function* should be defined that needs to be minimized over all weights and biases of the network.

In precipitation detection, the network needs to provide an output of a three dimensional vector containing probabilities associated with each precipitation label. In particular, let the input to the last layer  $L$  be  $\mathbf{v}_i \in \mathbb{R}^D$ . The  $d^{\text{th}}$  component  $v_i^d$  shall be large when  $\mathbf{T}_{b_i}^c$  belongs to  $d^{\text{th}}$  precipitation category. This intuition is encoded by the SoftMax operator

$$\sigma_{\text{SM}}(v_i^d) = \frac{\exp(v_i^d)}{\sum_{d=1}^D \exp(v_i^d)},$$

that magnifies the large components of  $\mathbf{v}_i$  and maps them onto a probability simplex with positive values that sum to unity.

In the last layer, the output of the SoftMax function should be as close as possible to unity in component  $d$ , when  $\mathbf{T}_{b_i}^c$  belongs to label  $d^{\text{th}}$ . Therefore, we need a cost function that minimizes the distance between the outputs of the network and one-hot vector of labels in the probability space. The categorical cross-entropy is a common cost function for this purpose

$$\mathcal{J}(\theta) = -\frac{1}{M} \sum_{i=1}^M \left( \sum_{d=1}^D t_i^d \ln(\sigma_{\text{SM}}[v_i^d(\theta)]) \right),$$

where  $\theta$  is a vector representation of all unknown weights  $\mathbf{W}^{[2:L]}$  and biases  $\mathbf{b}^{[2:L]}$ .

When it comes to e-DNN, all layer use a Rectified Linear Unit (ReLU) activation function

$$\sigma_{\text{ReLU}}(z_i) = \begin{cases} 0 & z_i \leq 0, \\ z_i & z_i > 0, \end{cases}$$

where  $z_i$  is the input to  $i$ th neuron in a specific layer.

The cost function for estimation of precipitation rate in e-DNNs is chosen as follows:

$$\mathcal{J}(\theta) = \frac{1}{M} \sum_{i=1}^M \|\mathcal{F}(\theta) - r_i\|_p^p,$$

where  $r_i$  is observed surface precipitation rate, and  $\|\cdot\|_p^p$  is the  $p$ -norm of a vector. For estimation of rainfall rate, we set  $p = 1$ , while  $p = 2$  is considered for snowfall. The reason for departing from classic least-squares ( $p = 2$ ) for estimation of rainfall rate is due to heavier tail structure of rainfall than snowfall. The rainfall data have large extreme rates that can make the estimations prone to biases, when a least-squares loss is used.

### 3.2.3. Training Algorithm

In this paper, we use the Root Mean Squared Propagation (RMSProp) (Hinton et al., 2012), which is an extension to the Adaptive Gradient descent (AdaGrad) (Duchi et al., 2011) algorithm to minimize the aforementioned cost functions. These algorithms both rely on the stochastic steepest gradient descent (Robbins and Monro, 1951; Bottou, 2012) approach; however, the RMSProp modifies AdaGrad in a way that increases the chance of finding the global minimum, when the cost function is highly non-convex. In a general setting, the use of a steepest descent approach involves two main steps: (i) calculation of the expectation of the gradient vector over all training data points and (ii) a proper choice of learning rate or step size  $\eta$  to assure a computationally efficient convergence.

As the size of the network and/or training data grows, the first step becomes computationally prohibitive and an optimal choice of  $\eta$  becomes more important for a successful training. The stochastic gradient approach provides a cheap alternative by approximating the expected value of the gradients only over a much smaller number of randomly selected training data points. To that end, the training dataset is usually shuffled randomly and split into some mini-batches of size  $M' \ll M$ . Here, we use different batch sizes from 500 to 2000 for the detection and estimation networks through trial and error analyses.

### 3.2.4. Overfitting and Regularization

Note that only 1E+6 number of these coincidences over land and oceans are used for tuning the network parameters. To avoid overfitting, we split the tuning database of DPR and CPR coincidences into training (70%), validation (15%), and testing (15%) data sets. The training dataset is used for learning the unknown parameters in the network. After each training epoch, validation data are fed to the trained network and the error is measured. Initially both training and validation errors decrease until there is no improvement in

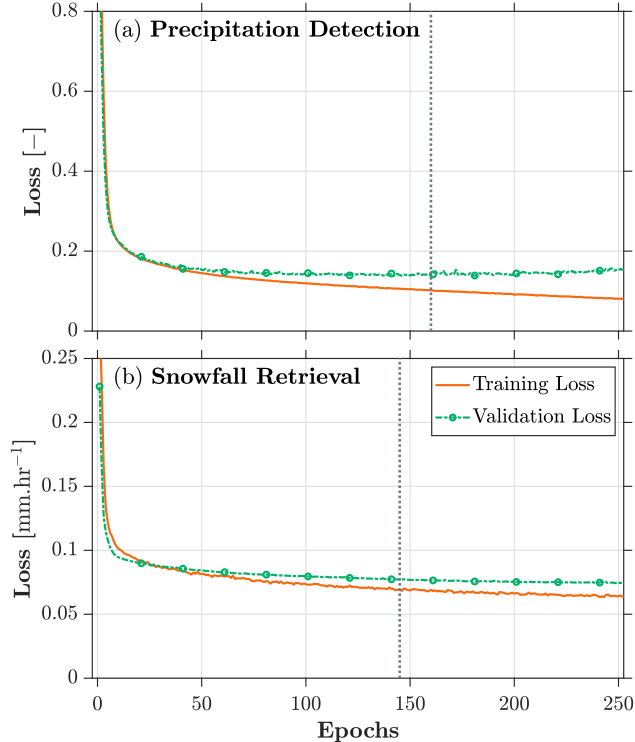


**Fig. 2.** Examples of loss function changes as a function of training epochs for (a) detection (d-DNN) and (b) estimation DNNs (e-DNN) using DPR database over oceans. The initial learning rates are set to  $1 \times 10^{-4}$  and  $1 \times 10^{-5}$ , respectively. To avoid overfitting, the learning process stops at the point where the validation loss does not decrease in the next 25 epochs.

the performance of the network on the validation dataset at which the training is stopped. Two examples are provided in Fig 2. The testing dataset is used to evaluate the performance of the network on an independent data not used before in the learning process. To further boost generalization capability of the DNNs, we used the “Dropout” regularization (Srivastava et al., 2014) that randomly ignores a fraction of neurons along with all its incoming and outgoing connections during the training process. Here, a dropout rate of 10% is considered at each training epoch.

### 3.2.5. Algorithmic Architecture

As explained previously, we propose a sequence of DNNs to first *detect* the surface precipitation occurrence and its phase and then *estimate* its near surface rate. This configuration is guided through the KerasTuner Python library (OMalley et al., 2019) that trains a network with different configurations and hyperparameters (e.g., number of hidden layers, neural

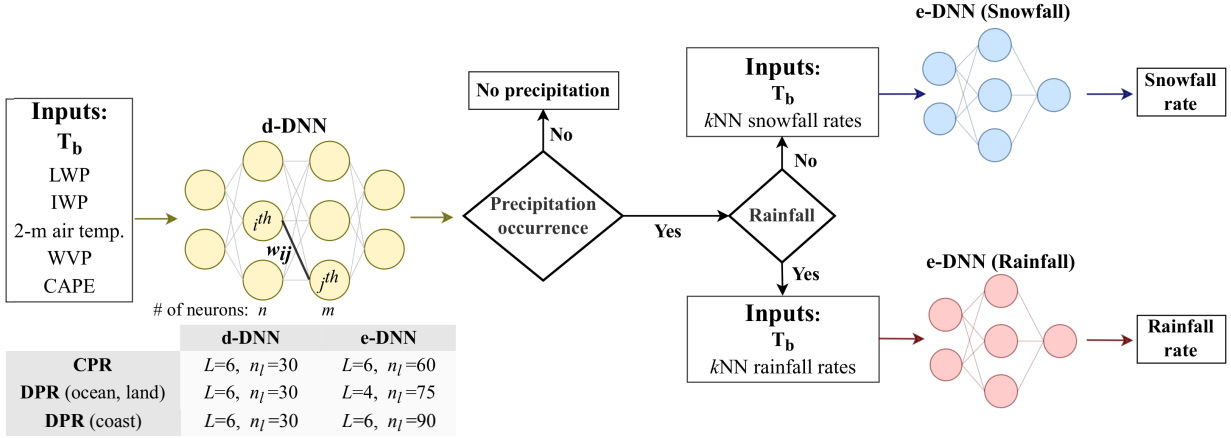


**Fig. 3.** The architecture of the Deep-learning precipitation rEtrieval alGOrithm (DIEGO) for a single *a priori* database over a specific surface type. As shown, a Deep Neural Network (DNN) first detects (d-DNN) the occurrence and phase of precipitation and then another one (e-DNN) estimates its rate. The inputs to the DNNs, number of layers  $L$ , and number neurons  $n_l$  in each layer are shown for different training databases in the table.

nodes) to find the best set of choices based on the defined cost function over a prespecified search space. The basic architecture of the algorithm is shown in Fig. 3 for a specific surface type. As shown, for each surface type, we have two d-DNNs and four e-DNNs to detect precipitation and its phase and estimate its rate using both DPR and CPR observations.

#### 4. Results and Discussion

The results of the algorithm are shown and discussed in three steps. First, we show the error metrics for the testing data sets. The results for orbital retrievals of a few selected storms including Winter Storm Grayson over the East Coast of the U.S., a snowstorm over Greenland, Hurricane Zeta over the Gulf of Mexico, and a storm over the Southern Indian Ocean. Lastly, we implement the algorithm for all GMI orbits in calendar year 2021 and compare its outputs with GPROF-V07 retrievals and ERA5 reanalysis data on an annual scale.

In a storm-scale, we also present combined retrievals through a simple fusion approach only at a storm-scale. When either of CPR or DPR d-DNNs detects precipitation, we label that pixel as precipitating. When the detected phase is different, the pixel is labeled as

mixed. It is important to note that, this does not literally imply a mixed phase precipitation and just represents a higher degree of retrieval uncertainty in terms of the detected phase by the two active databases. When only one of the d-DNNs detects precipitation, we retrieve its rate solely based on the sequenced e-DNN and use the results as the final retrieval. When both d-DNNs for CPR and DPR detect precipitation, the final rate is considered to be the mean of the estimated rates.

#### 4.1. Retrieval experiments using the test data sets

The test data sets are used to quantify intrinsic uncertainties in terms of detection and conditional estimation accuracy. The detection accuracy is quantified based on the True Positive Rate (TPR) or probability of detection and False Positive Rate (FPR) or probability of false alarm in Table. 1. In the table, we also report the results of  $k$ NN classification with  $k = 20$ , based on a majority vote rule, which was shown to be extremely effective in the PWM detection of precipitation and its phase (Ebtehaj et al., 2015a,c; Ebtehaj and Kummerow, 2017b; Vahedizade et al., 2021).

**Table 1:** Detection performance of DIEGO and  $k$ NN with  $k = 20$ . True Positive Rate (TPR) and False Positive Rate (FPR) are reported for retrievals based on both CloudSat CPR and GPM DPR testing databases.

	CPR						
	Ocean		Land		Coast		
	TPR	FPR	TPR	FPR	TPR	FPR	
$k$ NN	89.0	2.3	99.9	0.2	88.5	2.1	<b>Rain</b>
<b>DIEGO</b>	92.3	3.0	99.9	0.1	94.8	1.7	
$k$ NN	95.4	4.4	92.3	6.1	95.2	5.7	<b>Snow</b>
<b>DIEGO</b>	96.6	2.5	95.5	3.1	98.9	1.9	
	DPR						
$k$ NN	84.8	3.9	86.8	2.6	78.7	3.6	<b>Rain</b>
<b>DIEGO</b>	96.0	7.0	97.2	3.7	96.1	8.2	
$k$ NN	83.2	4.9	83.0	6.9	88.0	6.8	<b>Snow</b>
<b>DIEGO</b>	93.3	3.5	96.2	2.7	91.7	3.9	

The results show that the d-DNNs, with intrinsic classification capabilities as well as inclusion of relevant physical variables, generally provide a superior performance compared to  $k$ NN in detection of precipitation and its phase. Note that matching through  $k$ NN is

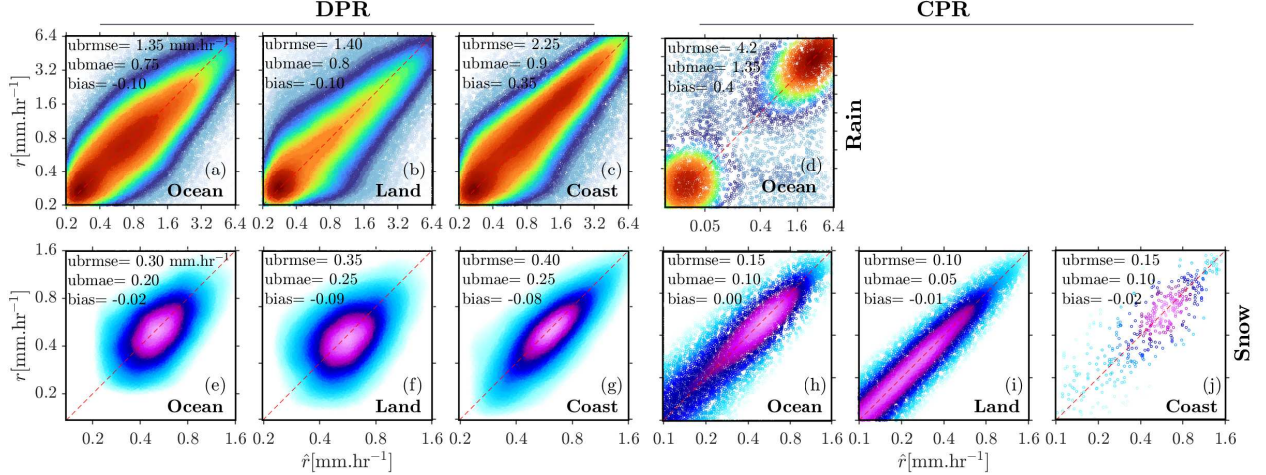


**Fig. 4.** Passive microwave retrievals of rainfall (a–d) and snowfall (e–j) by the DIEGO e-DNNs using the test databases for GPM DPR and CloudSat CPR. Variation of color from red–blue (blue–magenta) shows the variation of density of points from 0–1 in rainfall (snowfall) retrieval plots. The quality metrics are bias, unbiased root mean squared (ubrmse) and unbiased mean squared error (ubmae).

conducted only in the TB space. The probability of rainfall (snowfall) detection over oceans, using CPR data, reaches to almost 92 (97)%, while the probability of false alarm is below 3.0 (2.5)%. The CPR snowfall retrievals over land exhibit a TPR of  $\approx 95\%$  with the false alarm probability of less than 4%. For the DPR rainfall (snowfall), the TPR is above 96% (92%) over all land surfaces and is maximum over land 97.2 (96.2)%. The probability of false alarm is consistently below 8.0%, which is obtained for coastal rainfall. The FPR in detection of snowfall is slightly lower than rainfall using DPR databases and remains below 4% over land and oceans. Overall, we observe that the metrics are superior for rainfall (snowfall) retrievals when using the DPR (CPR) database.

The results of DIEGO e-DNNs are presented in Fig. 4 for both rainfall (top row) and snowfall (bottom row) conditional retrievals using DPR (first three columns) and CPR (last three columns) test databases – given that the precipitation is detected and its phase is properly determined. The statistics of the intrinsic uncertainties are reported for active retrievals below the 97.5th percentile to alleviate the effects of a few extreme values. As previously explained, the estimation results are not provided for CPR rainfall over land and coastal zones. It is important to note that the scatter plots are shown after applying a cumulative density function (CDF) matching to remove the reported biases. The CDF

matching functionals were learned from the testing databases for both CPR and DPR data. The most important observation is that PMW DPR rainfall retrievals are less uncertain than CPR rainfall over oceans. However, CPR snowfall retrievals exhibit less uncertainty than DPR snowfall, which also corroborate with the reported detection metrics in Table 1.

As reported in Fig. 4, the bias is relatively under control and is larger for rainfall than snowfall. Generally speaking, when the probability density function of the data is positively skewed, the estimators, which tend to regress towards the mean, lead to negative biases and vice versa. For example, the bias is negative in DPR precipitation retrievals over land and oceans except over coastal areas, which is around  $0.35 \text{ mm hr}^{-1}$ . Therefore, it appears that in these case, there are extremely light rainfall values that populate the testing data, which can be overestimated. However, the largest negative biases are over land, indicating the presence of more frequent extreme convective rainfalls events. The biases in snowfall retrievals are less than  $0.1 \text{ mm hr}^{-1}$  and slightly negative in majority of land surface types for both CPR and DPR – indicating that heavy snowfall events are underestimated; however, to a lesser extent than rainfall extremes.

The uncertainty of retrievals in terms of unbiased root mean squared error (ubrmse) and unbiased mean absolute error (ubmae) provides important information about the capability of the algorithm in retrieval of precipitation over different surface types. We can see that these uncertainty metrics are larger for rainfall than snowfall, which is expected as the probability distribution of rainfall is more heavy tailed. Overall, we observe that DPR (CPR) snowfall ubrmse is around 25 (4)% of the rainfall ubrmse. The maximum ubrmse for rainfall and snowfall belongs to CPR over ocean ( $4.2 \text{ mm hr}^{-1}$ ) and DPR over coast ( $0.4 \text{ mm hr}^{-1}$ ), respectively. The minimum ubrmse of  $0.10 \text{ mm hr}^{-1}$  is obtained for CPR snowfall retrievals over land. Once again, these observations indicate that intrinsically, DPR data lead to reduced uncertainty in retrieval of rainfall compared to CPR data, while this pattern is reverse when it comes to snowfall retrievals.

#### 4.2. Storm-scale retrieval experiments

Fig. 5 shows the results of the DIEGO applied on a GMI overpass (orbit #21882) capturing the powerful North American blizzard, known as the Winter Storm Grayson, that caused

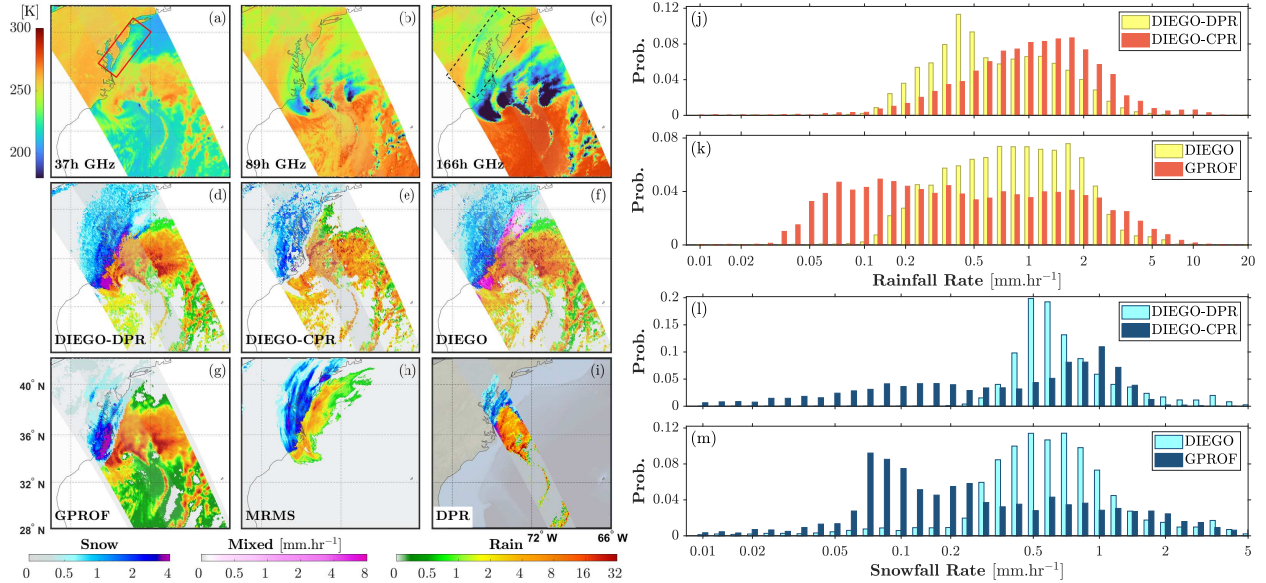


**Fig. 5.** Passive microwave retrievals (GPM orbit #21882) capturing the precipitation dumped by the Winter Storm Grayson on January 4, 2018 over the East Coasts of the United States. The GMI TBs at 37, 89 and 166 GHz horizontal polarization (a–c), precipitation retrievals by DIEGO (d–f), GPROF, MRMS, and DPR (g–i), as well as their corresponding probability histograms (j–m) at different phases.

widespread severe disruption and loss of life across the East Coast of the United States and Canada in early January 2018. Figs. 5a–c show the horizontally polarized TBs at 37, 89 and 166 GHz. Warmer signals of raindrop emission are apparent in 37 GHz over radiometrically cold Atlantic ocean. At higher frequencies, significant scattering signal or TB cooling is observed – indicating high concentration of ice aloft over ocean and the presence of a melting layer.

The results of DIEGO retrievals based on the DPR and CPR databases (Fig. 5d,e) are relatively consistent over ocean in terms of detected precipitation phase. The storm bands are properly captured in both retrievals. Even though, the DIEGO-CPR mean rainfall overestimates its DPR counterpart (Fig. 5j,k). Unlike DPR-based retrievals, those using the CPR database, show less variability as the rainfall rate remains almost constant across the central part of the storm and its trailing bands. For the retrieved rainfall values, the 97.5th percentile in DIEGO-CPR (-DPR) is 16.5 (9) mm hr<sup>-1</sup>; however, the 99.5th percentile is 38 (60) mm hr<sup>-1</sup>. In other words, while the bulk of the CPR-based retrievals overestimate the DPR counterpart, the extreme cells are more likely in DIEGO-DPR. We can clearly

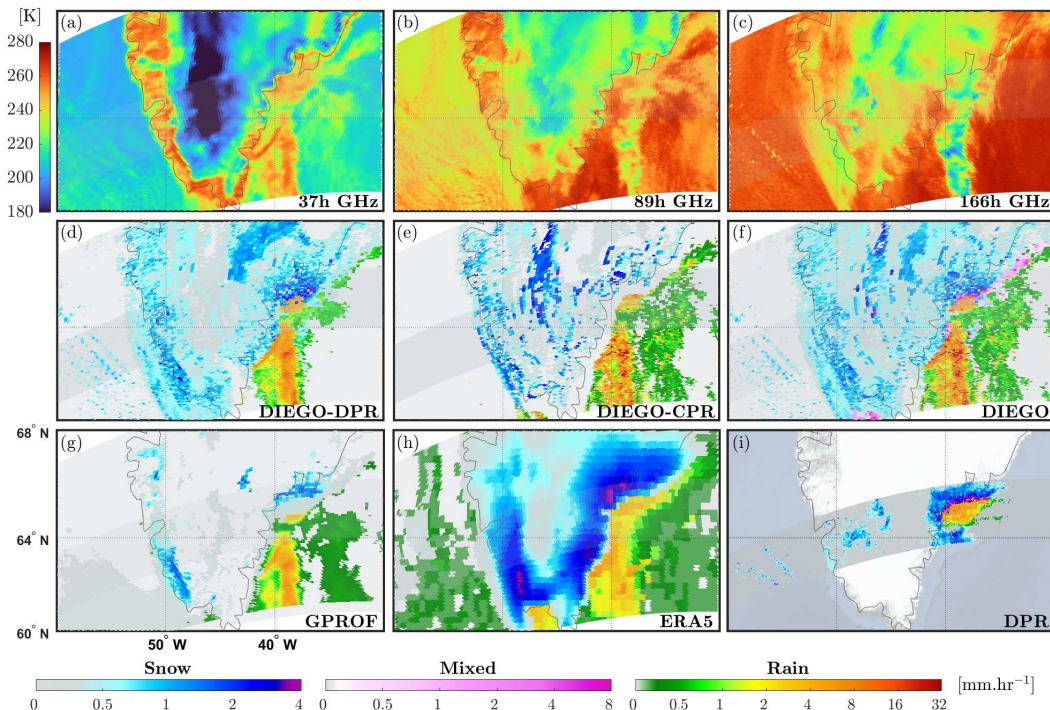


**Fig. 6.** Brightness temperatures by GMI (a–c), precipitation retrievals by DIEGO (d–f) and those from GPROF, ERA5, and DPR (G–I) for orbit #3080 on September 13, 2014 over Greenland.

see that the GPROF retrieves a wider range of rainfall variability with a flatter probability distribution and a large probability mass below  $0.1 \text{ mm hr}^{-1}$ , than DIEGO retrievals.

In the Delaware coastlines region, we clearly see that the warming signal in 37 GHz wanes down (shown within a red box), indicating that the rainfall is transitioning to snowfall from ocean to land. Visual inspection of 89 GHz TBs, shows that an outer band of depressed TB values is observed extending from southeast Chesapeake Bay to the Bald Head Island in North Carolina. This radiometrically cold band extends to northeast Pennsylvania in 166 GHz (shown within a black box), indicating the probability of overland snowfall. A large radiometrically cold area also exists in the 37 to 166 GHz observations over the northwest sector of the overpass over Pennsylvania. This features are likely due to ground snow cover and not precipitating snow.

All shown passive and active precipitation retrievals as well as MRMS (Fig. 5h) observations consistently indicate that the precipitation phase changes from liquid to solid as the storm moves from over ocean to land. The extent of snowfall occurrence is relatively consistent between DIEGO-DPR and -CPR. The DIEGO-CPR retrievals are less coherent

and patchier than DPR, which can be due to the fact that GMI-CPR coincidences included in the database are  $\pm 15$  minutes apart, which might lead to noisier CPR retrievals. As is evident, over the outer bands of the storm, the DIEGO-CPR retrieves lighter snowfall than DIEGO-DPR, which is more consistent with the MRMS data. A combined version of the retrievals is presented in (Fig. 5f). As explained previously, when CPR and DPR are inconsistent with respect to the detected phase, the retrievals are labeled as *mixed* and shown with a pink color map. As is evident, those mixed retrievals are mostly along the coastlines, where precipitation is changing its phase.

The probability histograms of DIEGO-DPR and -CPR snowfall retrievals, their combined version (DIEGO), as well as GPROF retrievals are shown in Fig. 5j–m. The mean snowfall in DIEGO-DPR is  $\sim 0.85$  mm hr<sup>-1</sup> while it is around 0.5 mm hr<sup>-1</sup> in DIEGO-CPR and thus, unlike the rainfall, snowfall is overestimated using DPR database. We can see the distribution of DIEGO-CPR is much wider than DIEGO-DPR and extends from 0.01 to 2 mm hr<sup>-1</sup>. The 97.5th percentiles are 3.5 and 1.5 mm hr<sup>-1</sup> and maximum retrieved values are 7.5 and 3 mm hr<sup>-1</sup>, for DIEGO-DPR and -CPR, respectively. Visual inspection of the histograms show that GPROF snowfall rates are largely concentrated below 0.1 mm hr<sup>-1</sup>, while a few extreme values exceeding 3 mm hr<sup>-1</sup> thicken the tail of the distribution significantly. These extreme values are largely extended from south of the Chesapeake Bay to the Pamlico Sound lagoon in North Carolina – shown with magenta color in Fig. 5g.

A complementary snowfall event at higher latitudes was also analyzed using GMI observations and various satellite-based retrievals. Fig. 6 shows a snowstorm over Greenland on September 13, 2014 (GMI orbit #3080). Passive microwave retrieval of precipitation over Greenland ice sheet can be challenging because of two main reasons. First, the background surface emission from a snow-covered ice sheet is different than majority of land surfaces. Thus, statistically speaking, there exist less coincidences of active/passive observations over this specific surface type and naturally the learned relationship between the TBs and surface precipitation can be more uncertain. Second, over a less emissive snow-covered ice, snowfall high-frequency scattering signatures can be weaker and the masking effects of supercooled cloud liquid water content can be stronger. In other words, under similar atmospheric conditions, the expected high frequency TB cooling for snowfall events over Greenland might be

less prominent compared to cases when snow falls over more emissive surfaces such as those covered by a vegetation canopy.

Visual inspection of 37 GHz channel (Fig. 6a) indicates increased TB values and thus potential occurrence of a rainfall events over the North Atlantic Ocean and Greenland Strait. This warm signal is accompanied with TB cooling in both 89 and 166 GHz – indicating ice aloft scattering and thus can show the presence of a melting layer. Over the southern and western coastlines, we observe a warming signal at 37 GHz, largely over ice free areas with a sub-arctic and tundra climate regimes. Perceptual interpretation of the TBs at high frequencies in response to the occurrence of precipitation is not straightforward due to the complexity of radiometric interactions of snow-covered ice with atmospheric signals – especially at 89 GHz, which is more sensitive to changes of surface emission than 166 GHz. Nevertheless, a cooling signal, likely due to the presence of ice particles and falling snow, is clearly visible over the southwest coastlines.

Although, it appears that as the storm moves over the ice sheet, the phase of precipitation transitions from liquid to solid, the snowfall retrievals are notably different across the shown products. The ERA5 simulations (Fig. 6h) indicate the occurrence of a snowstorm over southern Greenland along the coastlines. The intensity reaches to almost  $4 \text{ mm hr}^{-1}$  over the coastal areas and decays to zero in the middle of the ice sheet. While DIEGO retrievals also capture a coastal snowstorm, the retrieved rates are lower than ERA and some patchy snowfall cells are detected in the middle of ice sheet (Fig. 6d–f), which are not consistent between the DPR and CPR based retrievals. We suspect that the DPR database provides a more skillful detection capability over radiometrically complex surfaces due to higher number of samples of such conditions in its database. However, as shown in Fig. 1, the DPR-based snowfall retrievals are generally prone to overestimation compared to those of CPR.

To further demonstrate the performance of the proposed algorithm, precipitation retrievals for two additional orbits on October 10, 2014 (#3498) and October 28, 2020 (#37875) are shown in Fig. 7. Orbit #37875 captured the Hurricane Zeta that made landfall over Louisiana, United States. Overall, there is consistency between all shown retrievals. Here, we only show DIEGO-DPR because we have observed that the retrievals for intense rainstorms are more realistic using DPR than the CPR database as CPR reflectivity saturates.

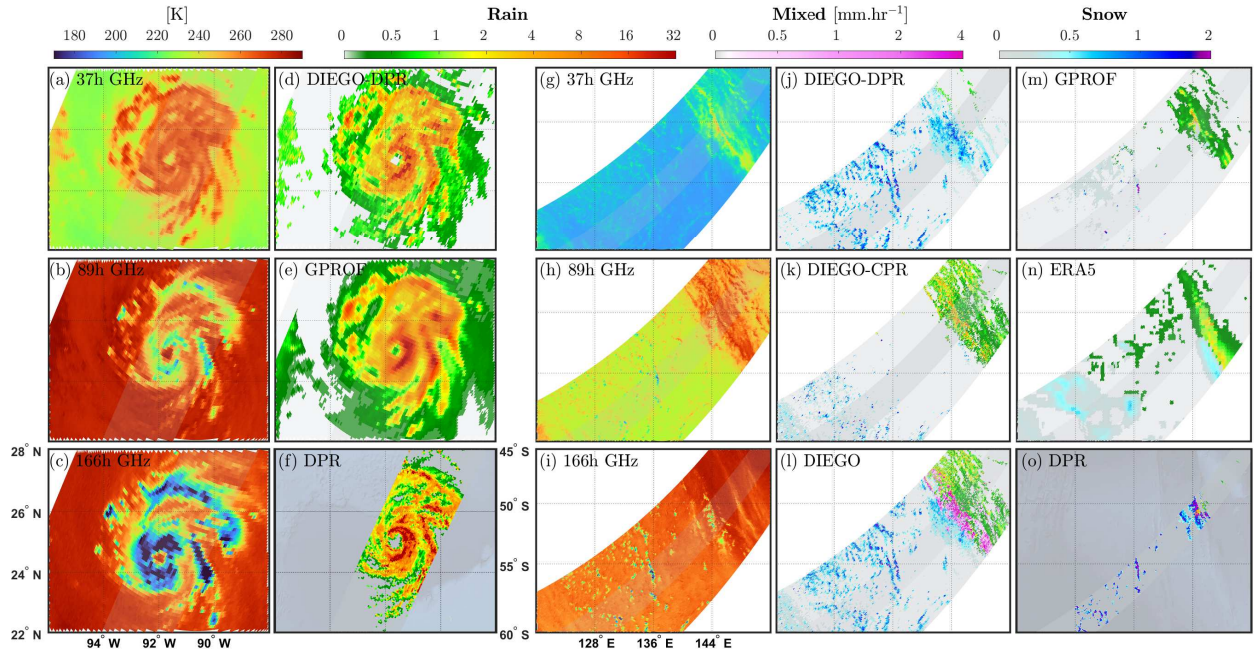


**Fig. 7.** Precipitation retrievals using the observed brightness temperatures for orbit #37875 on October 28, 2020 (Hurricane Zeta) and orbit #3498 on October 10, 2014.

As is evident, DIEGO-DPR captures the intensity of rainfall and its spatial band structure in a similar fashion as to GPROF and original DPR observations. As expected the intensities are generally underestimated for extreme values while the extent of lighter rainfall is overestimated compared to the active counterpart.

The results for orbit #3498 capturing a storm over the southwest Indian Ocean are different among the shown retrievals. Over the northeast part of the storm, 37 GHz observations show a warming signal indicating the possibility of a frontal precipitation event. Over higher frequency channels, there is no signature of ice scattering, except over the southern edge of the front – indicating that the clouds are largely warm, lifting is shallow, and potential precipitation is likely to be in liquid phase. The majority of retrievals indicate liquid precipitation over this part of the storm, including GPROF, DIEGO-CPR and ERA5, except the active DPR and passive DIEGO-DPR retrievals. Active DPR does not detect any rainfall and only catches snowfall events. Therefore, we conjecture that the observed discrepancies are not due to an algorithmic flaw but are rather related to intrinsic characteristics of the DPR training database. The DPR active retrievals use the reanalysis data of air temperature and moisture from the operational global analysis provided by the Japan Meteorological

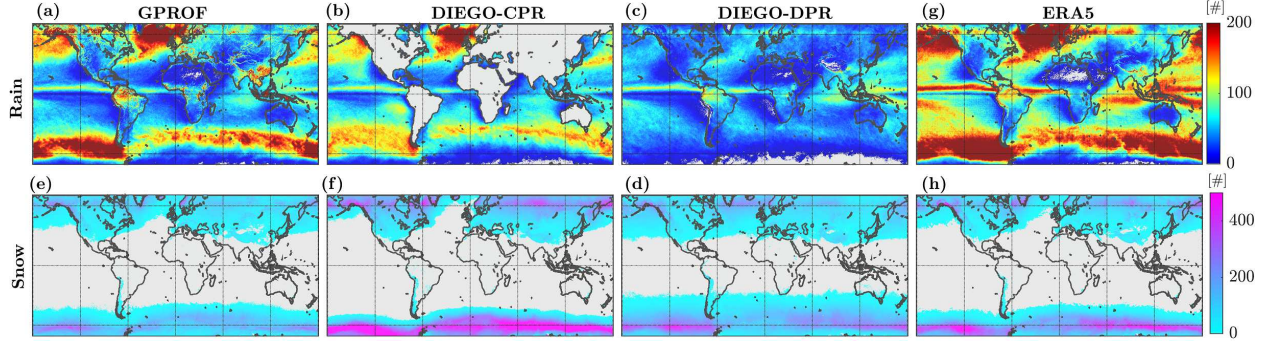


**Fig. 8.** Annual occurrence number of rainfall (top row) and snowfall (bottom row) in 2021 mapped onto a  $0.1^\circ$  grid box for GPROF (a, e), DNN-CPR (b, f), DIEGO-DPR (c, g), and ERA5 (d, h) products.

Agency, while CPR active retrievals rely on the ERA5 reanalysis data and use two different approach for phase determination. Even though, we fed the d-DNNs with ERA5 2-m air temperatures, it appears that the connections between TBs and precipitation phases learned from the DPR database significantly influence the final e-DNN outputs.

Over the southwest part of the orbit, weak sporadic warm signals exist at 37 GHz, which can be due to the presence of supercooled liquid water in the clouds. However, unlike the northern part of the storm, some of these warm signatures contain convective cold cells capturing significant high-frequency scattering signatures, perhaps due to the presence of localized convection. The shape of the signatures indicates possibilities of postfrontal cumuliform type clouds that contribute  $\sim 35\%$  of global snowfall events (Kulie et al., 2016). Sporadic snowfall is detected over those cells in all retrievals with different intensity values and extent. DIEGO-DPR retrieves more sporadic snowfall events over those high-frequency depressions with higher rates than the DIEGO-CPR, which is consistent with previous observations.

#### 4.3. Global-scale retrieval experiments

Throughout this subsection, we will compare the annual ERA5 data with the satellite retrievals. We should emphasize that ERA5 data should not be considered as a ground-truth; however, since the conservation of water and energy is satisfied in an Earth system model, its annual mean values might be considered as a relative reference for consistency assessment of satellite retrievals.

Figs. 8a–h show the annual frequency of rain and snowfall detection in 2021 for the rates above  $0.01 \text{ mm hr}^{-1}$  — considering all overpasses of GMI. Note that the ERA5 data, with a resolution of 30 km, are mapped onto the GMI grids using linear (nearest neighbor) interpolation in time (space). We did not retrieve any precipitation over sea ice as the number of DPR and CPR coincidences were not adequate for a robust training of the neural networks. Therefore, for a one-to-one comparison, we removed precipitation data from all products over sea ice.

As is evident, there are some discrepancies between the frequency of occurrences among the shown annual retrievals — especially for the rainfall data. The differences are expected, partly due to two main reasons. First, ERA5 cannot properly represent sub-grid scale convective precipitation processes. This leads to a representative error, and a positive bias in occurrences, especially for rainfall (Fig. 8a–d). Because any sub-grid occurrence of precipitation shall be represented with a lower rate across the entire ERA5 grids, to warrant an unbiased estimation. Beyond the middle latitudes, we still observe that ERA5 has higher frequency of occurrence over the Intertropical Convergence Zone (ITCZ) than all other satellite products, which further verify the provided reasoning. Second, precipitation radars cannot properly capture light precipitation, especially DPR retrievals that are limited to the rates greater than  $0.2 \text{ mm hr}^{-1}$ . As a result, large discrepancies are apparent over mid-latitude oceans, where the rainfall events are light but frequent. For example, we observe a zonal belt of high occurrences, in all products except DIEGO-DPR, over the south Pacific ocean around latitude  $50^\circ\text{S}$  that extends to the southern Atlantic and Indian oceans over latitudes  $30\text{--}40^\circ\text{S}$ .

Overall, for rainfall retrievals (Fig. 8a–d), we see that the occurrence frequency in DIEGO-DPR is less than 50% of ERA5 and GPROF in middle latitudes. We need to recall that the true positive rate of rainfall detection for DIEGO-DPR is more than 95% over land and oceans for controlled retrieval experiments (Tab.1). Therefore, passive retrievals based on DPR data can miss significant number of rainfall events. We need to note that detection deficiencies may not necessarily lead to significant underestimation in the total amount as shown later on in Fig. 9c. DPR retrievals often capture intense convective precipitation at a much higher resolution than the reanalysis data, which can compensate for missing

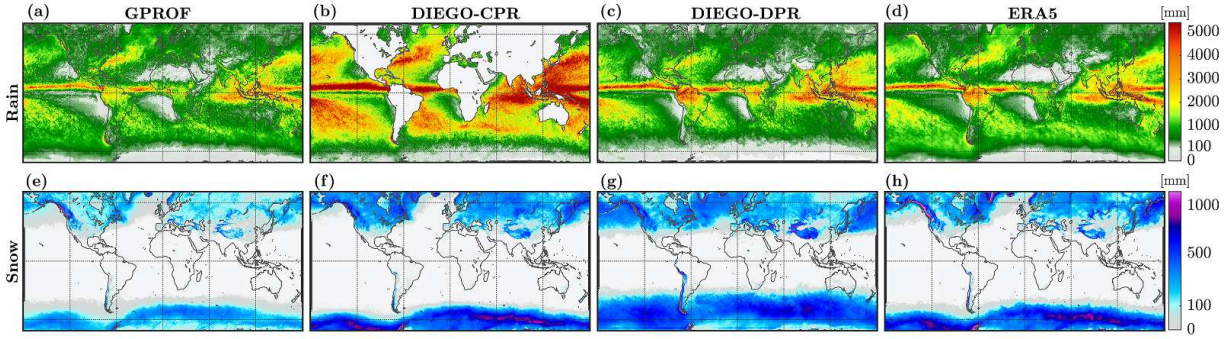


**Fig. 9.** Annual estimates of the total rainfall (top row) and snowfall (bottom row) (in millimeters) in 2021 at a  $0.1^\circ$  grid box for GPROF, DIEGO-CPR, DIEGO-DPR, and ERA5 products.

light rainfall when calculating total annual precipitation. The occurrence rates significantly increase for DIEGO-CPR as the database contains much lighter precipitation rates than the DPR. This indicates that even though the rainfall CPR database may not lead to unbiased rainfall retrievals with an expected dynamic range, it provides higher detection accuracy of light rainfall compared to the DPR database.

For snowfall (Fig. 8e–h), DIEGO-CPR provides the largest number of occurrences, which are apparent over the polar regions. The number and extent of occurrences are relatively consistent between DIEGO-CPR and ERA5 – perhaps because snowfall is less driven by intense convection and its dynamic range is narrower than rainfall. The lowest occurrence rates belong to DIEGO-DPR, however, the snowfall occurrences extend to lower latitudes and for example cover parts of the Southern Australia. Once again, as demonstrated in Fig. 9, small number of occurrences may not directly translate into a lesser amount of the total annual snowfall.

An estimate of total annual precipitation for all products is shown in Fig. 9. For the rainfall retrievals (Fig. 9a–d) there is consistency among all products except DIEGO-CPR, which significantly overestimates the global rainfall as previously discussed. Visual inspection shows that DIEGO-DPR slightly overestimates ERA5 and GPROF over the ITCZ where majority of rainfall events are convective; however, underestimates those products over lower latitudes where stratiform light rainfall can dominate precipitation regimes. This latitudinal trend is more clear in Fig. 10 that shows zonal mean of precipitation for a subset of selected

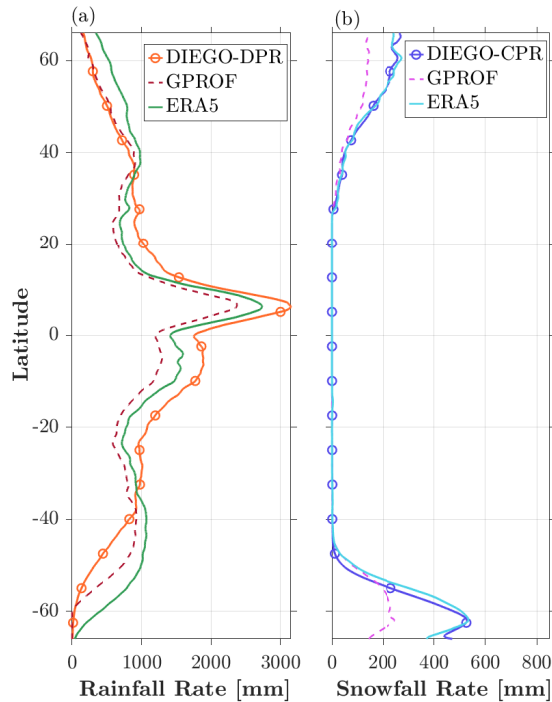


**Fig. 10.** Annual rainfall (a) and snowfall (b) zonal mean values obtained from Fig. 9.

products. As shown, above  $35^\circ$  S-N, DIEGO-DPR underestimates both ERA5 and GPROF and overestimate them within the tropics.

The results of annual snowfall (Fig. 9e–h) show marked differences between the products both over land and oceans. Overall, it appears that DIEGO-DPR (GPROF) overestimates (underestimate) snowfall both over land and oceans, compared to other products. There is a reasonable degree of agreement between DIEGO-CPR and ERA5 data both over oceans and land. For example, over Eurasia and Tibetan Plateau, the annual retrievals both in terms of spatial patterns and magnitude are closely similar while GPROF significantly underestimate both ERA5 and DIEGO-CPR. The snow depth climatology of Eurasia (Bormann et al., 2018; He et al., 2018) indicates that on average we should expect 50 cm of snow over Siberia, which is consistent with DIEGO-CPR.

However, over some areas covered with shallow seasonal snow-cover, such as the Canadian Prairie, we observed that DIEGO retrievals, for both CPR and DPR databases, overestimate other products. Recent research (Rahimi et al., 2022) shows that over shallow snow cover with minimal emerging vegetation, where the depth is less than 10–15 cm, the PMW

retrieval of snowfall can be excessively sensitive to change of snow layering and grain size distribution. Therefore, snow cover continues to be a major challenge for snowfall retrievals over land and sea ice and stratification of the database, based on the snow types and physical characteristics, can lead to reduced uncertainties even when a deep neural network is deployed. Nevertheless, the zonal mean of snowfall retrievals (Fig. 10b) also indicates that DIEGO-CPR and ERA5 retrievals are in a close agreement. Over the Northern Hemisphere, we suspect that the overestimation by DIEGO-CPR is largely related to those snowfall events over snow-covered surfaces.

We need to emphasize that in Fig. 9, the retrieval of DIEGO-DPR snowfall retrievals are biased corrected. In Appendix A, the positively biased retrievals are shown and compared with active DPR data over the GPM inner swath (see Fig. A.1 in Appendix A). This overestimation can be caused by multiple reasons: i) The distribution of snowfall in DPR dataset is not heavy tailed with its mean value significantly higher than snowfall in CPR dataset. ii) The phase variable of 2A-DPR dataset is determined at the lowest radar range gate uncontaminated by surface clutters, which may be 0.5–2.0 km above the surface (even over oceans). Therefore, the actual phase might be different those retrieved more near the surface. iii) 2A-DPR detects more snowfall over ocean in the northern hemisphere compared to the other products, especially over the Norwegian and Greenland Sea. These snowfall values paired with their observed TBs are included in the training dataset and can affect the detection and estimation performance of DIEGO-DPR. To remove the existing bias, the snowfall retrieval of DIEGO-DPR are modified using a scale factor by dividing the latitudinal mean of active DPR snowfall retrievals by latitudinal mean of passive DPR snowfall retrievals, which can also be applied to the orbital retrievals as well.

## 5. Summary and Conclusion

In this paper, we examined a deep and dense neural network architecture that learns from coincidences of passive/active observations from the Global Precipitation Measurement (GPM) core satellite microwave imager (GMI), the W-band *CloudSat* Profiling Radar (CPR), and the Dual-frequency Precipitation Radar (DPR) onboard GPM. The algorithm can properly condition the retrievals to key cloud microphysical and environmental variables

that are tightly linked to the occurrence, phase and rate of precipitation including the cloud liquid and ice water path, total water vapor content, 2-m air temperature, and convective potential energy – obtained from ERA5 reanalysis data. This architecture first detects the occurrence of precipitation, determines its phase, and then estimates its rate through a series of two deep neural networks.

Overall, under controlled numerical experiments, reported in Table 1, we observed that DIEGO can improve detection of precipitation and its phase beyond previous Bayesian retrieval algorithms that have used  $k$ -nearest neighbor ( $k$ NN) matching techniques and neural network based approaches. However, the tested deep neural networks were unable to properly estimate the precipitation rate with an acceptable uncertainty – solely from a pixel-level observed vector of brightness temperatures and other ancillary inputs. To reduce the uncertainty, the networks were fed with precipitation rates associated with  $k$ -nearest vectors of brightness temperatures in the training databases.

Overall, evaluating the retrievals for multiple storms and assessing their annual values in 2021, the following key points are worth noting. (i) It is recommended that the coincident CPR snowfall data will be used in any future attempts for improving official algorithms or in new snowfall data products as recommended in other previous research as well (Panegrossi et al., 2017; Ebtehaj et al., 2020; Sanò et al., 2022). However, current CPR rainfall data (version 5) shall be only used for detection of rainfall and using them in the context of either Bayesian or deep learning retrieval algorithms might lead to over estimation. (ii) The coincidences of active snowfall retrievals from DPR shall be used with caution in any passive microwave retrieval algorithm as it might lead to significant overestimation of snowfall. (iii) A thorough validation of satellite snowfall retrievals is essential. The ground-based observations from the National Centers for Environmental Prediction (NCEP) Automated Data Processing (ADP) and the International Comprehensive Ocean–Atmosphere Data Set (ICOADS) can be used for such a validation as suggested in (Sims and Liu, 2015). A software tool, which reproduces the main results of the paper, is made publicly available at: (<https://github.com/aebtehaj/DIEGO>)

## Acknowledgment

The research is primarily supported by grants from NASA’s Remote Sensing Theory program (RST, 80NSSC20K1717) through Dr. Lucia Tsaoussi and NASA’s Interdisciplinary Research in Earth Science (IDS) program (IDS, 80NSSC20K1294) through Dr. Will McCarty and Dr. Aaron Piña. Authors would like to thank Dr. F. Joseph Turk for providing CloudSat-GPM coincidence dataset, and Dr. Mircea Greu for providing feedback on the algorithm and the results of this research paper.

## Appendix A. Debiasing DIEGO-DPR snowfall retrievals

To be able to compare DIEGO-DPR snowfall retrievals with active DPR retrievals, the snowfall estimations of DIEGO-DPR are mapped onto the 2A-DPR Ku-band footprint and the total amount of snowfall is calculated in 2021 (Fig. A.1). The DIEGO-DPR shows overestimation both over land and ocean compare to the active DPR retrievals because of the explained reasons in the text. In order to mitigate this bias, a latitudinal bias correction factor is calculated by dividing the zonal mean values of 2A-DPR snowfall by the DIEGO-DPR.

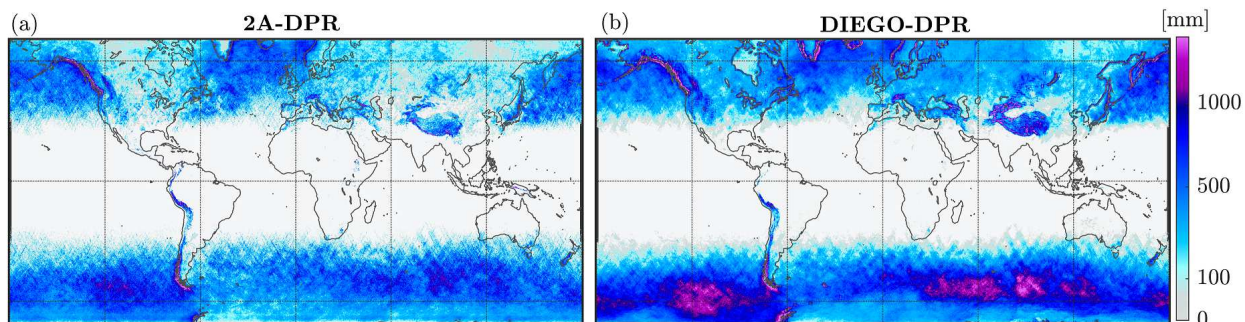


**Fig. A.1.** Annual estimates of the total snowfall in 2021 mapped onto a  $0.1^\circ$  grid box for DPR, and DIEGO-DPR products.

## References

F. Aires, C. Prigent, W. B. Rossow, and M. Rothstein. A new neural network approach including first guess for retrieval of atmospheric water vapor, cloud liquid water path,

- surface temperature, and emissivities over land from satellite microwave observations. *Journal of Geophysical Research: Atmospheres*, 106:14887–14907, 7 2001. ISSN 01480227. doi: 10.1029/2001JD900085. URL <http://doi.wiley.com/10.1029/2001JD900085>.
- P. M. Atkinson and A. R. L. Tatnall. Introduction neural networks in remote sensing. *International Journal of Remote Sensing*, 18:699–709, 3 1997. ISSN 0143-1161. doi: 10.1080/014311697218700.
- Peter Bauer, Paul Amayenc, Christian D. Kummerow, and Eric A. Smith. Over-ocean rainfall retrieval from multisensor data of the tropical rainfall measuring mission. part ii: Algorithm implementation. *Journal of Atmospheric and Oceanic Technology*, 18:1838–1855, 11 2001. ISSN 0739-0572. doi: 10.1175/1520-0426(2001)018<1838:OORRFM>2.0.CO;2.
- Ali Behrangi, Matthew Christensen, Mark Richardson, Matthew Lebsock, Graeme Stephens, George J Huffman, David Bolvin, Robert F Adler, Alex Gardner, Bjorn Lambrigtsen, and Eric Fetzer. Status of high-latitude precipitation estimates from observations and reanalyses. *Journal of Geophysical Research: Atmospheres*, 121:4468–4486, 5 2016. ISSN 2169-897X. doi: 10.1002/2015JD024546. URL <https://doi.org/10.1002/2015JD024546>. doi: 10.1002/2015JD024546.
- Y. Bengio. Learning deep architectures for ai. *Foundations and Trends® in Machine Learning*, 2:1–127, 2009. ISSN 1935-8237. doi: 10.1561/2200000006. URL <http://www.nowpublishers.com/article/Details/MAL-006>.
- R. Bennartz and P. Bauer. Sensitivity of microwave radiances at 85-183 GHz to precipitating ice particles. *Radio Science*, 38(4), 2003. ISSN 00486604. doi: 10.1029/2002RS002626. URL <http://doi.wiley.com/10.1029/2002RS002626>.
- Ralf Bennartz and Grant W. Petty. The Sensitivity of Microwave Remote Sensing Observations of Precipitation to Ice Particle Size Distributions. *Journal of Applied Meteorology*, 40(3):345–364, 2001. ISSN 0894-8763. doi: 10.1175/1520-0450(2001)040<0345:TSOMRS>2.0.CO;2.

- Ralf Bennartz, Frank Fell, Claire Pettersen, Matthew D. Shupe, and Dirk Schuettemeyer. Spatial and temporal variability of snowfall over greenland from cloudsat observations. *Atmospheric Chemistry and Physics*, 19:8101–8121, 6 2019. ISSN 1680-7324. doi: 10.5194/acp-19-8101-2019.
- Wesley Berg. Gpm gmi common calibrated brightness temperatures collocated l1c 1.5 hours 13 km v05. *Greenbelt, MD, USA, Goddard Earth Sciences Data and Information Services Center (GES DISC)*, 2016. doi: <https://doi.org/10.5067/GPM/GMI/GPM/1C/05>.
- Christopher M Bishop. *Pattern Recognition and Machine Learning (Information Science and Statistics)*. Springer-Verlag, 2006. ISBN 0387310738.
- Kat J. Bormann, Ross D. Brown, Chris Derksen, and Thomas H. Painter. Estimating snow-cover trends from space. *Nature Climate Change 2018 8:11*, 8(11): 924–928, 10 2018. ISSN 1758-6798. doi: 10.1038/s41558-018-0318-3. URL <https://www.nature.com/articles/s41558-018-0318-3>.
- Léon Bottou. Stochastic gradient learning in neural networks. 1991.
- Léon Bottou. *Stochastic Gradient Descent Tricks*. 2012. doi: 10.1007/978-3-642-35289-8\_25.
- Daniele Casella, Giulia Panegrossi, Paolo Sanò, Anna Cinzia Marra, Stefano Dietrich, Benjamin T Johnson, and Mark S Kulie. Evaluation of the GPM-DPR snowfall detection capability: Comparison with CloudSat-CPR. *Atmospheric Research*, 197:64–75, 2017.
- Haonan Chen, V. Chandrasekar, Robert Cifelli, and Pingping Xie. A machine learning system for precipitation estimation using satellite and ground radar network observations. *IEEE Transactions on Geoscience and Remote Sensing*, 58: 982–994, 2 2020. ISSN 0196-2892. doi: 10.1109/TGRS.2019.2942280. URL <https://ieeexplore.ieee.org/document/8861302/>.
- Ofer Dekel, Ran Gilad-Bachrach, Ohad Shamir, and Lin Xiao. Optimal distributed online prediction using mini-batches. *Journal of Machine Learning Research*, 13, 2012. ISSN 1532-4435.

- Li Deng, Geoffrey Hinton, and Brian Kingsbury. New types of deep neural network learning for speech recognition and related applications: an overview. pages 8599–8603. IEEE, 5 2013. ISBN 978-1-4799-0356-6. doi: 10.1109/ICASSP.2013.6639344.
- Zhipeng Deng, Hao Sun, Shilin Zhou, Juanping Zhao, Lin Lei, and Huanxin Zou. Multi-scale object detection in remote sensing imagery with convolutional neural networks. *ISPRS Journal of Photogrammetry and Remote Sensing*, 145:3–22, 11 2018. ISSN 09242716. doi: 10.1016/j.isprsjprs.2018.04.003.
- David W Draper, David A Newell, Frank J Wentz, Sergey Krimchansky, and Gail M Skofronick-Jackson. The global precipitation measurement (gpm) microwave imager (gmi): Instrument overview and early on-orbit performance. *IEEE Journal of Selected Topics in Applied Earth Observations and Remote Sensing*, 8:3452–3462, 7 2015. ISSN 1939-1404. doi: 10.1109/JSTARS.2015.2403303. URL <http://ieeexplore.ieee.org/document/7052302/>.
- John Duchi, Elad Hazan, and Yoram Singer. Adaptive subgradient methods for online learning and stochastic optimization. *Journal of Machine Learning Research*, 12:2121–2159, 7 2011.
- C. E. Duchon and C. J. Biddle. Undercatch of tipping-bucket gauges in high rain rate events. *Advances in Geosciences*, 25:11–15, 3 2010. ISSN 1680-7359. doi: 10.5194/adgeo-25-11-2010.
- A. M. Ebtehaj and C. D. Kummerow. Microwave retrievals of terrestrial precipitation over snow-covered surfaces: A lesson from the gpm satellite. *Geophysical Research Letters*, 44:6154–6162, 6 2017a. ISSN 0094-8276. doi: 10.1002/2017GL073451. URL <https://onlinelibrary.wiley.com/doi/10.1002/2017GL073451>.
- A.M. M. Ebtehaj and C.D. D. Kummerow. Microwave retrievals of terrestrial precipitation over snow-covered surfaces: A lesson from the GPM satellite. *Geophysical Research Letters*, 44(12), 6 2017b. doi: 10.1002/2017GL073451. URL <http://doi.wiley.com/10.1002/2017GL073451>.

- Ardeshir Ebtehaj, Christian D. Kummerow, and F. Joseph Turk. Metric learning for approximation of microwave channel error covariance: Application for satellite retrieval of drizzle and light snowfall. *IEEE Transactions on Geoscience and Remote Sensing*, 58:903–912, 2 2020. ISSN 0196-2892. doi: 10.1109/TGRS.2019.2941682. URL <https://ieeexplore.ieee.org/document/8858045/>.
- Ardeshir M Ebtehaj, Rafael L. Bras, and Efi Foufoula-Georgiou. Shrunk Locally Linear Embedding for Passive Microwave Retrieval of Precipitation. *IEEE Trans. Geosci. Remote.*, 53(7):3720–3736, 7 2015a. ISSN 0196-2892. doi: 10.1109/TGRS.2014.2382436.
- Ardeshir M. Ebtehaj, Rafael L. Bras, and Efi Foufoula-Georgiou. Shrunk locally linear embedding for passive microwave retrieval of precipitation. *IEEE Transactions on Geoscience and Remote Sensing*, 53:3720–3736, 7 2015b. ISSN 0196-2892. doi: 10.1109/TGRS.2014.2382436. URL <http://ieeexplore.ieee.org/document/7010030/>.
- Ardeshir M Ebtehaj, Rafael L Bras, and Efi Foufoula-Georgiou. Evaluation of ShARP Passive Rainfall Retrievals over Snow-covered Land Surfaces and Coastal Zones. *J. Hydrometeor*, 3 2015c. ISSN 1525-755X. doi: 10.1175/JHM-D-15-0164.1. URL <http://dx.doi.org/10.1175/JHM-D-15-0164.1>.
- Ardeshir M. Ebtehaj, Rafael L. Bras, and Efi Foufoula-Georgiou. Evaluation of sharp passive rainfall retrievals over snow-covered land surfaces and coastal zones. *Journal of Hydrometeorology*, 17:1013–1029, 4 2016. ISSN 1525-755X. doi: 10.1175/JHM-D-15-0164.1. URL <http://journals.ametsoc.org/doi/10.1175/JHM-D-15-0164.1>.
- K. Franklin Evans and Graeme L. Stephens. Microwave radiative transfer through clouds composed of realistically shaped ice crystals. part i. single scattering properties. *Journal of the Atmospheric Sciences*, 52:2041–2057, 6 1995. ISSN 0022-4928. doi: 10.1175/1520-0469(1995)052<2041:MRTTCC>2.0.CO;2.
- T. Fuchs, J. Rapp, F. Rubel, and B. Rudolf. Correction of synoptic precipitation observations due to systematic measuring errors with special regard to precipitation phases. *Physics and Chemistry of the Earth, Part B: Hydrology, Oceans and Atmosphere*, 26:689–693, 1 2001. ISSN 14641909. doi: 10.1016/S1464-1909(01)00070-3.

Xavier Glorot and Yoshua Bengio. Understanding the difficulty of training deep feedforward neural networks. pages 249–256, 2010. URL <http://www.iro.umontreal>.

Ian Goodfellow, Yoshua Bengio, and Aaron Courville. *Deep Learning*. MIT Press, 2017.

Vesta Afzali Goroooh, Ata Akbari Asanjan, Phu Nguyen, Kuolin Hsu, and Soroosh Sorooshian. Deep neural network high spatiotemporal resolution precipitation estimation (deep-step) using passive microwave and infrared data. *Journal of Hydrometeorology*, 2 2022. ISSN 1525-755X. doi: 10.1175/JHM-D-21-0194.1.

Mircea Grecu and William S. Olson. Bayesian estimation of precipitation from satellite passive microwave observations using combined radar–radiometer retrievals. *Journal of Applied Meteorology and Climatology*, 45:416–433, 3 2006. ISSN 1558-8432. doi: 10.1175/JAM2360.1.

Mircea Grecu, William S. Olson, and Emmanouil N. Anagnostou. Retrieval of precipitation profiles from multiresolution, multifrequency active and passive microwave observations. *Journal of Applied Meteorology*, 43:562–575, 4 2004. ISSN 0894-8763. doi: 10.1175/1520-0450(2004)043<0562:ROPPFM>2.0.CO;2.

Mircea Grecu, William S. Olson, Stephen Joseph Munchak, Sarah Ringerud, Liang Liao, Ziad Haddad, Bartie L. Kelley, and Steven F. McLaughlin. The gpm combined algorithm. *Journal of Atmospheric and Oceanic Technology*, 33:2225–2245, 10 2016. ISSN 0739-0572. doi: 10.1175/JTECH-D-16-0019.1. URL [https://journals.ametsoc.org/view/journals/atot/33/10/jtech-d-16-0019\\_1.xml](https://journals.ametsoc.org/view/journals/atot/33/10/jtech-d-16-0019_1.xml).

Clement Guilloteau, Efi Foufoula-Georgiou, Pierre Kirstetter, Jackson Tan, and George J. Huffman. How well do multi-satellite products capture the space-time dynamics of precipitation? part i: five products assessed via a wavenumber-frequency decomposition. *Journal of Hydrometeorology*, 8 2021. ISSN 1525-755X. doi: 10.1175/JHM-D-21-0075.1.

Clément Guilloteau and Efi Foufoula-Georgiou. Beyond the pixel: Using patterns and multi-scale spatial information to improve the retrieval of precipitation from spaceborne passive

microwave imagers. *Journal of Atmospheric and Oceanic Technology*, 37:1571–1591, 9 2020. ISSN 0739-0572. doi: 10.1175/JTECH-D-19-0067.1.

Atsushi Hamada and Yukari N Takayabu. Improvements in detection of light precipitation with the global precipitation measurement dual-frequency precipitation radar (gpm dpr). *Journal of Atmospheric and Oceanic Technology*, 33:653–667, 2016. doi: 10.1175/JTECH-D-15-0097.1. URL [https://journals.ametsoc.org/view/journals/atot/33/4/jtech-d-15-0097\\_1.xml](https://journals.ametsoc.org/view/journals/atot/33/4/jtech-d-15-0097_1.xml).

John M Haynes, Tristan S L’Ecuyer, Graeme L Stephens, Steven D Miller, Cristian Mitrescu, Norman B Wood, and Simone Tanelli. Rainfall retrieval over the ocean with spaceborne w-band radar. *Journal of Geophysical Research: Atmospheres*, 114, 4 2009. ISSN 0148-0227. doi: 10.1029/2008JD009973. URL <https://doi.org/10.1029/2008JD009973>. doi: 10.1029/2008JD009973.

Qiong He, Zhiyan Zuo, Renhe Zhang, and Ruonan Zhang. Seasonal prediction and predictability of Eurasian spring snow water equivalent in NCEP Climate Forecast System version 2 reforecasts. *Climate Dynamics*, 50(1-2):339–348, 1 2018. ISSN 14320894. doi: 10.1007/S00382-017-3611-3/FIGURES/7. URL <https://link.springer.com/article/10.1007/s00382-017-3611-3>.

Hans Hersbach, Bill Bell, Paul Berrisford, Shoji Hirahara, András Horányi, Joaquín Muñoz-Sabater, Julien Nicolas, Carole Peubey, Raluca Radu, Dinand Schepers, Adrian Simons, Cornel Soci, Saleh Abdalla, Xavier Abellan, Gianpaolo Balsamo, Peter Bechtold, Gionata Biavati, Jean Bidlot, Massimo Bonavita, Giovanna Chiara, Per Dahlgren, Dick Dee, Michail Diamantakis, Rossana Dragani, Johannes Flemming, Richard Forbes, Manuel Fuentes, Alan Geer, Leo Haimberger, Sean Healy, Robin J. Hogan, Elías Hólm, Marta Janisková, Sarah Keeley, Patrick Laloyaux, Philippe Lopez, Cristina Lupu, Gabor Radnoti, Patricia Rosnay, Iryna Rozum, Freja Vamborg, Sebastien Villaume, and Jean-Noël Thépaut. Era5 hourly data on single levels from 1979 to present. copernicus climate change service (c3s) climate data store (cds). (accessed on 03-2021). 2018. doi: 10.24381/cds.adbb2d47.

- Andrew Heymsfield, Aaron Bansemer, Norman B. Wood, Guosheng Liu, Simone Tanelli, Ousmane O. Sy, Michael Poellot, and Chuntao Liu. Toward improving ice water content and snow-rate retrievals from radars. part ii: Results from three wavelength radar–collocated in situ measurements and cloud-sat–gpm–trmm radar data. *Journal of Applied Meteorology and Climatology*, 57:365–389, 2 2018. ISSN 1558-8424. doi: 10.1175/JAMC-D-17-0164.1. URL <https://journals.ametsoc.org/jamc/article/57/2/365/107579/Toward-Improving-Ice-Water-C>
- Geoffrey Hinton, Nitish Srivastava, and Kevin Swersky. Neural networks for machine learning lecture 6a overview of mini-batch gradient descent, 2012.
- Yang Hong, Kuo-Lin Hsu, Soroosh Sorooshian, and Xiaogang Gao. Precipitation estimation from remotely sensed imagery using an artificial neural network cloud classification system. *Journal of Applied Meteorology*, 43:1834–1853, 12 2004. ISSN 1520-0450. doi: 10.1175/JAM2173.1. URL <https://journals.ametsoc.org/doi/10.1175/JAM2173.1>.
- Arthur Y Hou, Ramesh K Kakar, Steven Neeck, Ardeshir A Azarbarzin, Christian D Kummerow, Masahiro Kojima, Riko Oki, Kenji Nakamura, and Toshio Iguchi. The global precipitation measurement mission. *Bulletin of the American Meteorological Society*, 95:701–722, 7 2014. ISSN 0003-0007. doi: 10.1175/BAMS-D-13-00164.1. URL <https://doi.org/10.1175/BAMS-D-13-00164.1>.
- Toshio Iguchi, Shinta Seto, Robert Meneghini, Naofumi Yoshida, Jun Awaka, Takuji Kubota, Toshiaki Kozu, V. Chandra, Minda Le, Liang Liao, Simone Tanelli, and Steve Durden. An overview of the precipitation retrieval algorithm for the dual-frequency precipitation radar (dpr) on the global precipitation measurement (gpm) mission’s core satellite. page 85281C, 11 2012. doi: 10.1117/12.977352.
- Toshio Iguchi, Shinta Seto, Robert Meneghini, Naofumi Yoshida, Jun Awaka, and Takuji Kubota. Gpm / dpr level-2 algorithm theoretical basis document. 2018. URL [https://gpm.nasa.gov/sites/default/files/2019-05/ATBD\\_DPR\\_201811\\_with\\_Appendix3b.pdf](https://gpm.nasa.gov/sites/default/files/2019-05/ATBD_DPR_201811_with_Appendix3b.pdf).
- Sergey Ioffe and Christian Szegedy. Batch normalization: Accelerating deep network training by reducing internal covariate shift. 2 2015. URL <http://arxiv.org/abs/1502.03167>.

- Chris Kidd and George Huffman. Global precipitation measurement. *Meteorological Applications*, 18:334–353, 9 2011. ISSN 13504827. doi: 10.1002/met.284.
- Dalia B. Kirschbaum, George J. Huffman, Robert F. Adler, Scott Braun, Kevin Garrett, Erin Jones, Amy McNally, Gail Skofronick-Jackson, Erich Stocker, Huan Wu, and Benjamin F. Zaitchik. Nasa’s remotely sensed precipitation: A reservoir for applications users. *Bulletin of the American Meteorological Society*, 98:1169–1184, 6 2017. ISSN 0003-0007. doi: 10.1175/BAMS-D-15-00296.1.
- Pierre-Emmanuel Kirstetter, Y. Hong, J. J. Gourley, S. Chen, Z. Flamig, J. Zhang, M. Schwaller, W. Petersen, and E. Amitai. Toward a Framework for Systematic Error Modeling of Spaceborne Precipitation Radar with NOAA/NSSL Ground Radar-Based National Mosaic QPE. *Journal of Hydrometeorology*, 2012. ISSN 1525-755X. doi: 10.1175/jhm-d-11-0139.1.
- Mark S Kulie and Lisa Milani. Seasonal variability of shallow cumuliform snowfall: A cloud-sat perspective. *Quarterly Journal of the Royal Meteorological Society*, 144:329–343, 11 2018. ISSN 0035-9009. doi: 10.1002/qj.3222. URL <https://doi.org/10.1002/qj.3222>. doi: 10.1002/qj.3222.
- Mark S Kulie, Ralf Bennartz, Thomas J Greenwald, Yong Chen, and Fuzhong Weng. Uncertainties in microwave properties of frozen precipitation: Implications for remote sensing and data assimilation. *Journal of the Atmospheric Sciences*, 67:3471–3487, 2010. doi: 10.1175/2010JAS3520.1. URL <https://journals.ametsoc.org/view/journals/atmsoc/67/11/2010jas3520.1.xml>.
- Mark S. Kulie, Lisa Milani, Norman B. Wood, Samantha A. Tushaus, Ralf Bennartz, and Tristan S. L’Ecuyer. A shallow cumuliform snowfall census using spaceborne radar. *Journal of Hydrometeorology*, 2016. ISSN 15257541. doi: 10.1175/JHM-D-15-0123.1.
- Christian Kummerow. Gpm gmi (gprof) radiometer precipitation profiling l2a 1.5 hours 13 km v05. *Greenbelt, MD, Goddard Earth Sciences Data and Information Services Center (GES DISC)*, 2016.

- C Kummerow, W S Olson, and L Giglio. A simplified scheme for obtaining precipitation and vertical hydrometeor profiles from passive microwave sensors. *IEEE Transactions on Geoscience and Remote Sensing*, 34:1213–1232, 1996. ISSN 1558-0644 VO - 34. doi: 10.1109/36.536538.
- Christian Kummerow, William Barnes, Toshiaki Kozu, James Shiue, and Joanne Simpson. The tropical rainfall measuring mission (trmm) sensor package. *Journal of Atmospheric and Oceanic Technology*, 15:809–817, 6 1998. ISSN 0739-0572. doi: 10.1175/1520-0426(1998)015<0809:TTRMMT>2.0.CO;2.
- Christian Kummerow, Y. Hong, W. S. Olson, S. Yang, R. F. Adler, J. McCollum, R. Ferraro, G. Petty, D-B. Shin, and T. T. Wilheit. The evolution of the goddard profiling algorithm (gprof) for rainfall estimation from passive microwave sensors. *Journal of Applied Meteorology*, 40:1801–1820, 11 2001. ISSN 0894-8763. doi: 10.1175/1520-0450(2001)040<1801:TEOTGP>2.0.CO;2.
- Christian D. Kummerow, Sarah Ringerud, Jody Crook, David Randel, and Wesley Berg. An observationally generated a priori database for microwave rainfall retrievals. *Journal of Atmospheric and Oceanic Technology*, 28:113–130, 2 2011. ISSN 1520-0426. doi: 10.1175/2010JTECHA1468.1.
- Christian D. Kummerow, David L. Randel, Mark Kulie, Nai-Yu Wang, Ralph Ferraro, S. Joseph Munchak, and Veljko Petkovic. The evolution of the goddard profiling algorithm to a fully parametric scheme. *Journal of Atmospheric and Oceanic Technology*, 32:2265–2280, 12 2015. ISSN 0739-0572. doi: 10.1175/JTECH-D-15-0039.1.
- Yann LeCun, Yoshua Bengio, and Geoffrey Hinton. Deep learning. *Nature*, 521:436–444, 5 2015. ISSN 0028-0836. doi: 10.1038/nature14539. URL <http://www.nature.com/articles/nature14539>.
- Tristan S. L’Ecuyer and Graeme L. Stephens. An estimation-based precipitation retrieval algorithm for attenuating radars. *Journal of Applied Meteorology*, 41:272–285, 3 2002. ISSN 0894-8763. doi: 10.1175/1520-0450(2002)041<0272:AEBPRA>2.0.CO;2.

- Vincenzo Levizzani and Elsa Cattani. Satellite remote sensing of precipitation and the terrestrial water cycle in a changing climate. *Remote Sensing*, 11:2301, 10 2019. ISSN 2072-4292. doi: 10.3390/rs11192301.
- Shutao Li, Weiwei Song, Leyuan Fang, Yushi Chen, Pedram Ghamisi, and Jon Atli Benediktsson. Deep learning for hyperspectral image classification: An overview. *IEEE Transactions on Geoscience and Remote Sensing*, 57:6690–6709, 9 2019. ISSN 0196-2892. doi: 10.1109/TGRS.2019.2907932. URL <https://ieeexplore.ieee.org/document/8697135/>.
- Ying Li, Haokui Zhang, Xizhe Xue, Yenan Jiang, and Qiang Shen. Deep learning for remote sensing image classification: A survey. *WIREs Data Mining and Knowledge Discovery*, 8, 11 2018. ISSN 1942-4787. doi: 10.1002/widm.1264.
- Yuei-An Liou, Y.C. Tzeng, and K.S. Chen. A neural-network approach to radiometric sensing of land-surface parameters. *IEEE Transactions on Geoscience and Remote Sensing*, 37:2718–2724, 1999. ISSN 01962892. doi: 10.1109/36.803419. URL <http://ieeexplore.ieee.org/document/803419/>.
- Guosheng Liu. Deriving snow cloud characteristics from cloudsat observations. *Journal of Geophysical Research: Atmospheres*, 113, 4 2008. ISSN 0148-0227. doi: 10.1029/2007JD009766. URL <https://doi.org/10.1029/2007JD009766>. doi: 10.1029/2007JD009766.
- Guosheng Liu and Judith A. Curry. Determination of characteristic features of cloud liquid water from satellite microwave measurements. *Journal of Geophysical Research: Atmospheres*, 98:5069–5092, 3 1993. ISSN 01480227. doi: 10.1029/92JD02888.
- Guosheng Liu and Judith A. Curry. Precipitation characteristics in greenland-iceland-norwegian seas determined by using satellite microwave data. *Journal of Geophysical Research: Atmospheres*, 102:13987–13997, 6 1997. ISSN 01480227. doi: 10.1029/96JD03090.
- Tristan S L’Ecuyer and Jonathan H Jiang. Touring the atmosphere aboard the a-train. *Physics Today*, 63:36–41, 7 2010. ISSN 0031-9228. doi: 10.1063/1.3463626. URL <https://doi.org/10.1063/1.3463626>. doi: 10.1063/1.3463626.

- Sergey Y. Matrosov and Alessandro Battaglia. Influence of multiple scattering on cloudsat measurements in snow: A model study. *Geophysical Research Letters*, 36:L12806, 6 2009. ISSN 0094-8276. doi: 10.1029/2009GL038704.
- Jorge J. Moré. *The Levenberg-Marquardt algorithm: Implementation and theory*. 1978. doi: 10.1007/BFb0067700.
- S. Joseph Munchak, Sarah Ringerud, Ludovic Brucker, Yalei You, Iris de Gelis, and Catherine Prigent. An active–passive microwave land surface database from gpm. *IEEE Transactions on Geoscience and Remote Sensing*, 58:6224–6242, 9 2020. ISSN 0196-2892. doi: 10.1109/TGRS.2020.2975477. URL <https://ieeexplore.ieee.org/document/9027116/>.
- Vinod Nair and Geoffrey E. Hinton. Rectified linear units improve restricted boltzmann machines. pages 807–814. Omnipress, 2010.
- Ali Bou Nassif, Ismail Shahin, Imtinan Attili, Mohammad Azzeh, and Khaled Shaalan. Speech recognition using deep neural networks: A systematic review. *IEEE Access*, 7: 19143–19165, 2019. ISSN 2169-3536. doi: 10.1109/ACCESS.2019.2896880.
- William S. Olson, Christian D. Kummerow, Gerald M. Heymsfield, and Louis Giglio. A method for combined passive and active microwave retrievals of cloud and precipitation profiles. *Journal of Applied Meteorology*, 35:1763–1789, 10 1996. ISSN 0894-8763. doi: 10.1175/1520-0450(1996)035<1763:AMFCPM>2.0.CO;2. URL [http://journals.ametsoc.org/doi/10.1175/1520-0450\(1996\)035<1763:AMFCPM>2.0.CO;2](http://journals.ametsoc.org/doi/10.1175/1520-0450(1996)035<1763:AMFCPM>2.0.CO;2).
- Tom OMalley, Elie Bursztein, James Long, Francois Chollet, Haifeng Jin, and Luca Invernizzi. Kerastuner. 2019. URL <https://github.com/keras-team/keras-tuner>.
- Giulia Panegrossi, Jean-François Rysman, Daniele Casella, Anna Marra, Paolo Sanò, and Mark Kulie. Cloudsat-based assessment of gpm microwave imager snowfall observation capabilities. *Remote Sensing*, 9:1263, 12 2017. ISSN 2072-4292. doi: 10.3390/rs9121263.
- G. W. Petty. Physical retrievals of over-ocean rain rate from multichannel microwave imagery. Part II: Algorithm implementation. *Meteorology and Atmospheric Physics*, 1994. ISSN 01777971. doi: 10.1007/BF01030054.

- G. W. Petty. Dimensionality reduction in bayesian estimation algorithms. *Atmospheric Measurement Techniques*, 6:2267–2276, 9 2013a. ISSN 1867-8548. doi: 10.5194/amt-6-2267-2013.
- G W Petty. Geoscientific Instrumentation Methods and Data Systems Dimensionality reduction in Bayesian estimation algorithms. *Atmos. Meas. Tech*, 6:2267–2276, 2013b. doi: 10.5194/amt-6-2267-2013. URL [www.atmos-meas-tech.net/6/2267/2013/](http://www.atmos-meas-tech.net/6/2267/2013/).
- Grant W Petty and Wei Huang. Microwave Backscatter and Extinction by Soft Ice Spheres and Complex Snow Aggregates. *Journal of the Atmospheric Sciences*, 67(67):769–787, 2010. ISSN 0022-4928. doi: 10.1175/2009JAS3146.1.
- Grant W. Petty and Ke Li. Improved passive microwave retrievals of rain rate over land and ocean. part i: Algorithm description. *Journal of Atmospheric and Oceanic Technology*, 30:2493–2508, 11 2013. ISSN 0739-0572. doi: 10.1175/JTECH-D-12-00144.1.
- Simon Pfreundschuh, Patrick Eriksson, David Duncan, Bengt Rydberg, Nina Håkansson, and Anke Thoss. A neural network approach to estimating a posteriori distributions of bayesian retrieval problems. *Atmospheric Measurement Techniques*, 11: 4627–4643, 8 2018. ISSN 1867-8548. doi: 10.5194/amt-11-4627-2018. URL <https://amt.copernicus.org/articles/11/4627/2018/>.
- S. Platnick, M.D. King, S.A. Ackerman, W.P. Menzel, B.A. Baum, J.C. Riedi, and R.A. Frey. The modis cloud products: algorithms and examples from terra. *IEEE Transactions on Geoscience and Remote Sensing*, 41:459–473, 2 2003. ISSN 0196-2892. doi: 10.1109/TGRS.2002.808301.
- Yue Qin. Global competing water uses for food and energy. *Environmental Research Letters*, 16:064091, 6 2021. ISSN 1748-9326. doi: 10.1088/1748-9326/ac06fa.
- Reyhaneh Rahimi, Ardeshir Ebtehaj, Giulia Panegrossi, Lisa Milani, Sarah E. Ringerud, and F. Joseph Turk. Vulnerability of Passive Microwave Snowfall Retrievals to Physical Properties of Snowpack: A Perspective From Dense Media Radiative Transfer Theory.

*IEEE Transactions on Geoscience and Remote Sensing*, 60, 2022. ISSN 15580644. doi: 10.1109/TGRS.2022.3184530.

Roy Rasmussen, Bruce Baker, John Kochendorfer, Tilden Meyers, Scott Landolt, Alexandre P. Fischer, Jenny Black, Julie M. Thériault, Paul Kucera, David Gochis, Craig Smith, Rodica Nitu, Mark Hall, Kyoko Ikeda, and Ethan Gutmann. How well are we measuring snow: The noaa/faa/ncar winter precipitation test bed. *Bulletin of the American Meteorological Society*, 93:811–829, 6 2012. ISSN 0003-0007. doi: 10.1175/BAMS-D-11-00052.1.

Herbert Robbins and Sutton Monro. A stochastic approximation method. *The Annals of Mathematical Statistics*, 22:400–407, 9 1951. ISSN 0003-4851. doi: 10.1214/aoms/1177729586.

F. Rosenblatt. The perceptron: A probabilistic model for information storage and organization in the brain. *Psychological Review*, 65:386–408, 1958. ISSN 1939-1471. doi: 10.1037/h0042519.

Jean François Rysman, Giulia Panegrossi, Paolo Sanò, Anna Cinzia Marra, Stefano Dietrich, Lisa Milani, and Mark S. Kulie. SLALOM: An All-Surface Snow Water Path Retrieval Algorithm for the GPM Microwave Imager. *Remote Sensing 2018, Vol. 10, Page 1278*, 10(8):1278, 8 2018. ISSN 2072-4292. doi: 10.3390/RS10081278. URL <https://www.mdpi.com/2072-4292/10/8/1278/htm><https://www.mdpi.com/2072-4292/10/8/1278>.

Jean-François Rysman, Giulia Panegrossi, Paolo Sanò, Anna Cinzia Marra, Stefano Dietrich, Lisa Milani, Mark S. Kulie, Daniele Casella, Andrea Camplani, Chantal Claud, and Léo Edel. Retrieving surface snowfall with the gpm microwave imager: A new module for the slalom algorithm. *Geophysical Research Letters*, 46:13593–13601, 11 2019. ISSN 0094-8276. doi: 10.1029/2019GL084576.

Paolo Sanò, Daniele Casella, Andrea Camplani, Leo Pio D’Adderio, and Giulia Panegrossi. A Machine Learning Snowfall Retrieval Algorithm for ATMS. *Remote Sensing 2022, Vol. 14, Page 1467*, 14(6):1467, 3 2022. ISSN 2072-4292. doi: 10.3390/RS14061467. URL <https://www.mdpi.com/2072-4292/14/6/1467/htm><https://www.mdpi.com/2072-4292/14/6/1467>.

Paolo Sanò, Giulia Panegrossi, Daniele Casella, Anna C. Marra, Francesco Di Paola, and Stefano Dietrich. The new passive microwave neural network precipitation retrieval (pnpr) algorithm for the cross-track scanning atms radiometer: description and verification study over europe and africa using gpm and trmm spaceborne radars. *Atmospheric Measurement Techniques*, 9:5441–5460, 11 2016. ISSN 1867-8548. doi: 10.5194/amt-9-5441-2016.

Paolo Sanò, Giulia Panegrossi, Daniele Casella, Anna Marra, Leo D’Adderio, Jean Rysman, and Stefano Dietrich. The passive microwave neural network precipitation retrieval (pnpr) algorithm for the conical scanning global microwave imager (gmi) radiometer. *Remote Sensing*, 10:1122, 7 2018. ISSN 2072-4292. doi: 10.3390/rs10071122. URL <http://www.mdpi.com/2072-4292/10/7/1122>.

Elizabeth M. Sims and Guosheng Liu. A Parameterization of the Probability of Snow–Rain Transition. *Journal of Hydrometeorology*, 16(4):1466–1477, 2015. ISSN 1525-755X. doi: 10.1175/JHM-D-14-0211.1. URL <http://journals.ametsoc.org/doi/abs/10.1175/JHM-D-14-0211.1>.

Gail Skofronick-Jackson and Benjamin T. Johnson. Surface and atmospheric contributions to passive microwave brightness temperatures for falling snow events. *Journal of Geophysical Research*, 116(D2):D02213, 1 2011. ISSN 0148-0227. doi: 10.1029/2010JD014438. URL <http://doi.wiley.com/10.1029/2010JD014438>.

Gail Skofronick-Jackson, Walter A Petersen, Wesley Berg, Chris Kidd, Erich F Stocker, Dalia B Kirschbaum, Ramesh Kakar, Scott A Braun, George J Huffman, Toshio Iguchi, Pierre E Kirstetter, Christian Kummerow, Robert Meneghini, Riko Oki, William S Olson, Yukari N Takayabu, Kinji Furukawa, and Thomas Wilhelm. The global precipitation measurement (gpm) mission for science and society. *Bulletin of the American Meteorological Society*, 98:1679–1695, 9 2017. ISSN 0003-0007. doi: 10.1175/BAMS-D-15-00306.1. URL <https://doi.org/10.1175/BAMS-D-15-00306.1>.

Gail Skofronick-Jackson, Mark Kulie, Lisa Milani, Stephen J Munchak, Norman B Wood, and Vincenzo Levizzani. Satellite estimation of falling snow: A global precipitation mea-

- surement (GPM) core observatory perspective. *Journal of applied meteorology and climatology*, 58(7):1429–1448, 2019.
- Gail M. Skofronick-Jackson, James R. Wang, Gerald M. Heymsfield, Robbie Hood, Will Manning, Robert Meneghini, and James A. Weinman. Combined radiometer–radar microphysical profile estimations with emphasis on high-frequency brightness temperature observations. *Journal of Applied Meteorology*, 42:476–487, 4 2003. ISSN 0894-8763. doi: 10.1175/1520-0450(2003)042<0476:CRRMPE>2.0.CO;2.
- Gail M. Skofronick-Jackson, Benjamin T. Johnson, and S. Joseph Munchak. Detection thresholds of falling snow from satellite-borne active and passive sensors. *IEEE Transactions on Geoscience and Remote Sensing*, 51:4177–4189, 7 2013. ISSN 0196-2892. doi: 10.1109/TGRS.2012.2227763.
- G.M. Skofronick-Jackson, Min-Jeong Kim, J.A. Weinman, and Dong-Eon Chang. A physical model to determine snowfall over land by microwave radiometry. *IEEE Transactions on Geoscience and Remote Sensing*, 42:1047–1058, 5 2004. ISSN 0196-2892. doi: 10.1109/TGRS.2004.825585.
- Soroosh Sorooshian, Kuo-Lin Hsu, Xiaogang Gao, Hoshin V. Gupta, Bisher Imam, and Dan Braithwaite. Evaluation of persiann system satellite–based estimates of tropical rainfall. *Bulletin of the American Meteorological Society*, 81:2035–2046, 9 2000. ISSN 0003-0007. doi: 10.1175/1520-0477(2000)081<2035:EOPSSE>2.3.CO;2. URL [http://journals.ametsoc.org/doi/10.1175/1520-0477\(2000\)081<2035:EOPSSE>2.3.CO;2](http://journals.ametsoc.org/doi/10.1175/1520-0477(2000)081<2035:EOPSSE>2.3.CO;2).
- Soroosh Sorooshian, Amir AghaKouchak, Phillip Arkin, John Eylander, Efi Foufoula-Georgiou, Russell Harmon, Jan M. H. Hendrickx, Bisher Imam, Robert Kuligowski, Brian Skahill, and Gail Skofronick-Jackson. Advancing the remote sensing of precipitation. *Bulletin of the American Meteorological Society*, 92:1271–1272, 10 2011. ISSN 0003-0007. doi: 10.1175/BAMS-D-11-00116.1.
- Nitish Srivastava, Geoffrey Hinton, Alex Krizhevsky, and Ruslan Salakhutdinov. Dropout: A simple way to prevent neural networks from overfitting. *Journal of Machine Learning Research*, 15:1929–1958, 2014.

- Graeme L. Stephens, Deborah G. Vane, Ronald J. Boain, Gerald G. Mace, Kenneth Sassen, Zhien Wang, Anthony J. Illingworth, Ewan J. O'connor, William B. Rossow, Stephen L. Durden, Steven D. Miller, Richard T. Austin, Angela Benedetti, and Cristian Mitrescu. The cloudsat mission and the a-train: A new dimension of space-based observations of clouds and precipitation. *Bulletin of the American Meteorological Society*, 83:1771–1790, 12 2002. ISSN 0003-0007. doi: 10.1175/BAMS-83-12-1771. URL <https://journals.ametsoc.org/view/journals/bams/83/12/bams-83-12-1771.xml>.
- Zeinab Takbiri, Ardeshir Ebtehaj, Efi Foufoula-Georgiou, Pierre-Emmanuel Kirstetter, and F. Joseph Turk. A prognostic nested k-nearest approach for microwave precipitation phase detection over snow cover. *Journal of Hydrometeorology*, 20:251–274, 2 2019. ISSN 1525-755X. doi: 10.1175/JHM-D-18-0021.1.
- Sagar K. Tamang, Ardeshir M. Ebtehaj, Andreas F. Prein, and Andrew J. Heymsfield. Linking global changes of snowfall and wet-bulb temperature. *Journal of Climate*, 33: 39–59, 1 2020. ISSN 0894-8755. doi: 10.1175/JCLI-D-19-0254.1.
- Guoqiang Tang, Yixin Wen, Jinyu Gao, Di Long, Yingzhao Ma, Wei Wan, and Yang Hong. Similarities and differences between three coexisting spaceborne radars in global rainfall and snowfall estimation. *Water Resources Research*, 53:3835–3853, 5 2017. ISSN 00431397. doi: 10.1002/2016WR019961. URL <http://doi.wiley.com/10.1002/2016WR019961>.
- Guoqiang Tang, Di Long, Ali Behrangi, Cunguang Wang, and Yang Hong. Exploring deep neural networks to retrieve rain and snow in high latitudes using multisensor and reanalysis data. *Water Resources Research*, 54:8253–8278, 10 2018. ISSN 0043-1397. doi: 10.1029/2018WR023830. URL <https://onlinelibrary.wiley.com/doi/abs/10.1029/2018WR023830>.
- F. J. Tapiador, C. Kidd, K.-L. Hsu, and F. Marzano. Neural networks in satellite rainfall estimation. *Meteorological Applications*, 11:83–91, 3 2004. ISSN 1350-4827. doi: 10.1017/S1350482704001173.
- Koichi Toyoshima, Hirohiko Masunaga, and Fumie A. Furuzawa. Early evaluation of ku- and ka-band sensitivities for the global precipitation mea-

surement (gpm) dual-frequency precipitation radar (dpr). *SOLA*, 11: 14–17, 2015. ISSN 1349-6476. doi: 10.2151/sola.2015-004. URL [https://www.jstage.jst.go.jp/article/sola/11/0/11\\_2015-004/\\_article](https://www.jstage.jst.go.jp/article/sola/11/0/11_2015-004/_article).

F J Turk, Sarah E Ringerud, Andrea Camplani, Daniele Casella, Randy J Chase, Ardeshir Ebtehaj, Jie Gong, Mark Kulie, Guosheng Liu, Lisa Milani, Giulia Panegrossi, Ramon Padullés, Jean-François Rysman, Paolo Sanò, Sajad Vahedizade, and Norman B Wood. Applications of a cloudsat-trmm and cloudsat-gpm satellite coincidence dataset. *Remote Sensing*, 13, 2021. doi: 10.3390/rs13122264.

F. Joseph Turk, Ziad S. Haddad, Pierre-Emmanuel Kirstetter, Yalei You, and Sarah Ringerud. An observationally based method for stratifying a priori passive microwave observations in a bayesian-based precipitation retrieval framework. *Quarterly Journal of the Royal Meteorological Society*, 144:145–164, 11 2018. ISSN 0035-9009. doi: 10.1002/qj.3203. URL <https://onlinelibrary.wiley.com/doi/abs/10.1002/qj.3203>.

S Vahedizade, A Ebtehaj, Y You, S E Ringerud, and F J Turk. Passive microwave signatures and retrieval of high-latitude snowfall over open oceans and sea ice: Insights from coincidences of gpm and cloudsat satellites. *IEEE Transactions on Geoscience and Remote Sensing*, pages 1–13, 2021. ISSN 1558-0644 VO -. doi: 10.1109/TGRS.2021.3071709.

Haohan Wang and Bhiksha Raj. On the origin of deep learning. 2 2017. URL <http://arxiv.org/abs/1702.07800>.

N B Wood, T S L’Ecuyer, F L Bliven, and G L Stephens. Characterization of video disdrometer uncertainties and impacts on estimates of snowfall rate and radar reflectivity. *Atmos. Meas. Tech.*, 6:3635–3648, 12 2013. ISSN 1867-8548. doi: 10.5194/amt-6-3635-2013.

Norman B Wood, Tristan S L’Ecuyer, Andrew J Heymsfield, Graeme L Stephens, David R Hudak, and Peter Rodriguez. Estimating snow microphysical properties using collocated multisensor observations. *Journal of Geophysical Research: Atmospheres*, 119:8941–8961, 7 2014. ISSN 2169-897X. doi: 10.1002/2013JD021303. URL <https://doi.org/10.1002/2013JD021303>. doi: 10.1002/2013JD021303.

- Munehiko Yamaguchi and Takuya Komori. Outline of the typhoon ensemble prediction system at the japan meteorological agency. *RSMC Tokyo-Typhoon Center Technical Review*, 11:14–24, 2009.
- Yalei You, Nai-Yu Wang, and Ralph Ferraro. A prototype precipitation retrieval algorithm over land using passive microwave observations stratified by surface condition and precipitation vertical structure. *Journal of Geophysical Research: Atmospheres*, 120:5295–5315, 6 2015. ISSN 2169-897X. doi: 10.1002/2014JD022534. URL <https://doi.org/10.1002/2014JD022534>. doi: 10.1002/2014JD022534.
- Yalei You, Nai-Yu Wang, Ralph Ferraro, and Scott Rudlosky. Quantifying the snowfall detection performance of the gpm microwave imager channels over land. *Journal of Hydrometeorology*, 18:729–751, 3 2017. ISSN 1525-755X. doi: 10.1175/JHM-D-16-0190.1.
- Jian Zhang, Kenneth Howard, Carrie Langston, Brian Kaney, Youcun Qi, Lin Tang, Heather Grams, Yadong Wang, Stephen Cockcks, Steven Martinaitis, Ami Arthur, Karen Cooper, Jeff Brogden, and David Kitzmilller. Multi-Radar Multi-Sensor (MRMS) quantitative precipitation estimation: Initial operating capabilities. *Bulletin of the American Meteorological Society*, 97(4):621–638, 2016. ISSN 00030007. doi: 10.1175/BAMS-D-14-00174.1.
- Zhong-Qiu Zhao, Peng Zheng, Shou-Tao Xu, and Xindong Wu. Object detection with deep learning: A review. *IEEE Transactions on Neural Networks and Learning Systems*, 30: 3212–3232, 11 2019. ISSN 2162-237X. doi: 10.1109/TNNLS.2018.2876865.